NANOROBOTS

Dual-responsive biohybrid neutrobots for active target delivery

Hongyue Zhang[1]*, Zesheng Li[1]*, Changyong Gao[2]*, Xinjian Fan[2], Yuxin Pang[3], Tianlong Li[2], Zhiguang Wu[1†], Hui Xie[2], Qiang He[1†]

Swimming biohybrid microsized robots (e.g., bacteria- or sperm-driven microrobots) with self-propelling and navigating capabilities have become an exciting field of research, thanks to their controllable locomotion in hard-to-reach areas of the body for noninvasive drug delivery and treatment. However, current cell-based microrobots are susceptible to immune attack and clearance upon entering the body. Here, we report a neutrophil-based microrobot ("neutrobot") that can actively deliver cargo to malignant glioma in vivo. The neutrobots are constructed through the phagocytosis of *Escherichia coli* membrane-enveloped, drug-loaded magnetic nanogels by natural neutrophils, where the *E. coli* membrane camouflaging enhances the efficiency of phagocytosis and also prevents drug leakage inside the neutrophils. With controllable intravascular movement upon exposure to a rotating magnetic field, the neutrobots could autonomously aggregate in the brain and subsequently cross the blood-brain barrier through the positive chemotactic motion of neutrobots along the gradient of inflammatory factors. The use of such dual-responsive neutrobots for targeted drug delivery substantially inhibits the proliferation of tumor cells compared with traditional drug injection. Inheriting the biological characteristics and functions of natural neutrophils that current artificial microrobots cannot match, the neutrobots developed in this study provide a promising pathway to precision biomedicine in the future.

INTRODUCTION

Swimming microrobots capable of autonomously propelling, navigating, and performing various complex tasks in body fluids are attracting a lot of attention (*1*–*10*). Inspired by motile microorganisms, such as bacteria, various types of swimming microrobots have been demonstrated to perform efficient locomotion in fluids, propelled by local chemical reactions or external physical stimuli, such as light, magnetic field, or acoustic field (*11*–*17*). Among them, magnetically actuated swimming microrobots hold great potential for active target delivery because they can be navigated into hard-to-reach tissues (*18*–*21*). Recent progress in magnetic swimming microrobots ranges from controllable propulsion of individuals to the emergence of swarms (*22*–*24*). Benefiting from precise control, a few magnetic microrobots have been used to achieve versatile biomedical tasks, including poration of cell membrane, targeted retention in the gastrointestinal tract, and ocular delivery (*25*–*28*). Although effective in conducting certain assignments, these swimming microrobots are susceptible to immune clearance once they have entered the body due to their foreign nature. These microrobots are unable to precisely seek the inflamed sites in complex environments in vivo and penetrate across biological barriers, such as the blood-brain barrier (BBB). Overall, it remains challenging to develop magnetically actuated swimming microrobots that can efficiently pass through various biological barriers to accomplish active target delivery (*29*–*32*).

Circulating blood cells have diverse and unique capabilities desirable for systemic delivery in biological environments, ranging from minor immunogenicity to chemotactic capacity. Such cells have inspired the pursuit of cell-hybrid swimming microrobots (*33*–*35*). Erythrocytes, for example, have been introduced into ultrasound-driven swimming microrobots and shown to prolong circulation in the bloodstream, owing to their biocompatibility and deformability in vivo (*36*). For targeted delivery applications, however, the penetration of biological barriers and homing locomotion toward sites of inflammation or pathogens are necessary capabilities. As a key mediator of the immune response, neutrophils (NEs) play an important role because of their activity in eliminating infectious threats through phagocytosis, degranulation, reactive oxygen species, and NE extracellular traps (NETs) (*37*, *38*). NEs can migrate across the BBB/blood-brain tumor barrier (BBB/BBTB) through chemotaxis along the gradient of inflammatory factors during inflammatory pathologies (*39*, *40*). Taking advantage of these properties, NEs have been developed as drug carriers to target inflamed tumors (*41*–*43*). Although chemotactic motion of these NEs to the tumor area and a reduction in tumor size have been observed, cancer in mice has not been fully cured using this method. This is largely because the drug-loading capacity, migration speed, and accumulation efficiency of existing NE-based carriers are limited. Therefore, engineering NE-based swimming microrobots with greatly enhanced drug-loading, motion, and navigation capabilities is expected to have good potential to achieve active delivery in vivo.

Here, we present dual-responsive (DR) hybrid NE microrobots, called neutrobots, capable of magnetically actuated intravascular motion and chemotactic behavior along the gradient of inflammatory factors to cross the BBB for active malignant glioma therapy in vivo (Fig. 1 and movie S1). These neutrobots encased paclitaxel (PTX)–loaded magnetic nanogels, which were coated with the outer membrane of *Escherichia coli* and then phagocytized by NEs. Thanks to the camouflaging provided by the *E. coli* membrane, the leakage of loaded drugs in the magnetic nanogels into NEs was prevented, endowing the neutrobots with biological activity similar to that of

[1]Key Laboratory of Microsystems and Microstructures Manufacturing (Ministry of Education), Harbin Institute of Technology, Harbin 150001, China. [2]State Key Laboratory of Robotics and System, Harbin Institute of Technology, Harbin 150001, China. [3]Department of Pathology, First Affiliated Hospital of Harbin Medical University, Harbin 150001, China.
*These authors contributed equally to this work.
†Corresponding author. Email: zhiguangwu@hit.edu.cn (Z.W.); qianghe@hit.edu.cn (Q.H.).

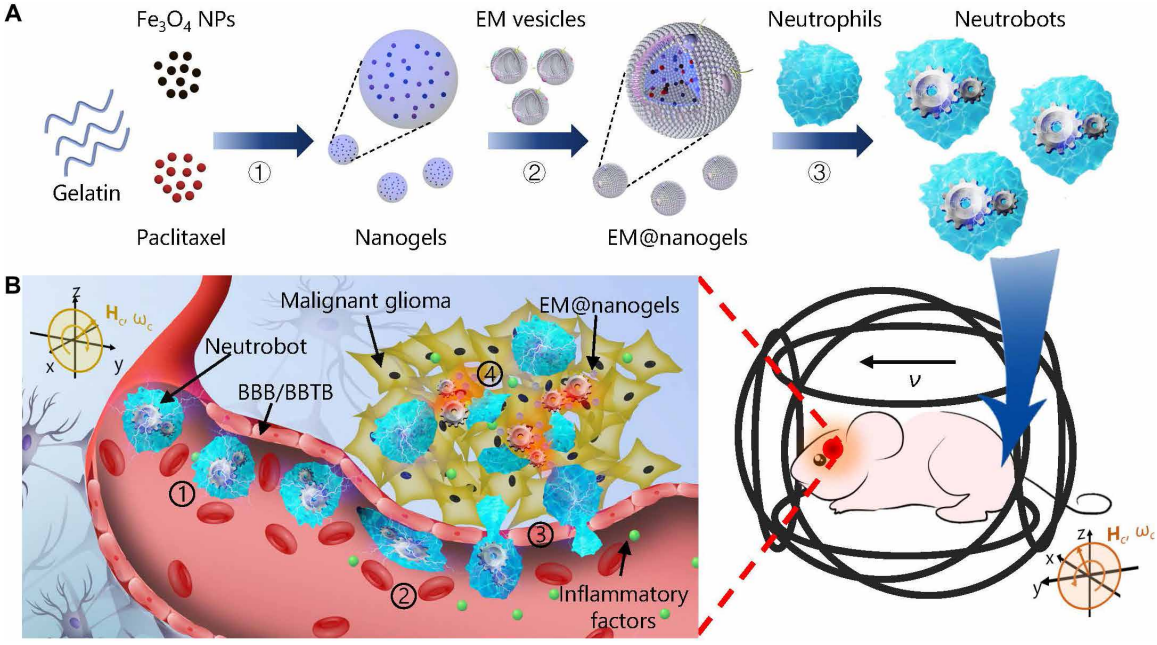

Fig. 1. Schematic of active therapeutics of dual-responsive neutrobots in vivo. (**A**) Schematic of the three-step fabrication of the neutrobots. ① Synthesis of the Fe_3O_4 NPs and PTX-loaded nanogels through emulsion/solvent evaporation method. ② Preparation of EM@nanogels by coextrusion technique. ③ Fabrication of neutrobots by phagocytosis of EM@nanogels into natural NEs. (**B**) Schematic of active delivery of dual-responsive neutrobots toward malignant glioma. ① Active accumulation of neutrobots close to glioma upon exposure to external magnetic field. BBB/BBTB, blood-brain barrier/blood-brain tumor barrier. ② Chemotaxis of the neutrobots along the gradient of inflammatory factors. ③ Penetration of the BBB of neutrobots through the natural capability of NEs. ④ PTX release from the neutrobots toward malignant glioma. $\boldsymbol{H}_c$, circular RMF; $\boldsymbol{\omega}_c$, critical frequency of RMF; $\boldsymbol{v}$, velocity of neutrobots.

natural NEs. The resulting neutrobots could not only accomplish controllable individual propulsion and swarm motion when exposed to a rotating magnetic field (RMF), but they could also operate efficiently in blood in vitro. Magnetic actuation notably accelerated the accumulation of neutrobots at the diseased sites in a model BBB in vitro, and chemotactic motion enabled the penetration of the BBB. The treatment of postoperative glioma with dual-responsive neutrobots further verified the active target delivery functionality in vivo; postoperative glioma was selected as the target because the surgical operation often leads to the recrudescence of tumor from residual tumor cells and local brain inflammation associated with the release of inflammatory factors. The gradient of released inflammatory factors triggered the chemotactic motion of neutrobots and, thus, the active therapy of postoperative glioma recurrence. The biohybrid neutrobots developed in this study exhibited the capability to harness the natural capabilities of NEs that would otherwise be difficult to replicate. Such dual-responsive neutrobots may advance the efficiency of active target delivery and noninvasive precision therapies.

RESULTS

Construction of neutrobots

The construction of dual-responsive hybrid neutrobots mainly consisted of three steps: synthesis of gelatin-based nanogels, preparation of *E. coli* membrane-coated nanogels (EM@nanogels), and phagocytosis of EM@nanogels by NEs as schematically illustrated in Fig. 1A. First, gelatin nanogels loaded with hydrophobic Fe_3O_4 nanoparticles (Fe_3O_4 NPs) and PTX were synthesized through an emulsion/solvent evaporation method (*44*). The encapsulated Fe_3O_4 NPs (~6 nm in diameter; fig. S1) were essential for controllable magnetic propulsion, and PTX was used as a model anticancer drug. The transmission electron microscopy (TEM) image in fig. S2 shows that the as-synthesized nanogels displayed a spherical geometry with an average diameter of ~97 nm, and each nanogel particle contained ~1800 Fe_3O_4 NPs. The loading dose of PTX in the nanogels was dependent on the amount of PTX used. When 1, 2, 4, 6, 8, and 10 mg of PTX were added, the loading per milligram of nanogel was estimated to be 57, 76, 86, 90, 118, and 183 μg, respectively (fig. S3). Second, the *E. coli* membranes were cloaked on the nanogel surface according to our previously reported procedures (*34*). Briefly, freshly purified outer membranes of *E. coli* were reassembled into *E. coli* membrane vesicles (EM vesicles), which were then fused onto the nanogel surface by using a coextruding method through a polycarbonate membrane with a diameter of 200 nm. The TEM image in Fig. 2A shows that the as-prepared EM@nanogels had a spherical geometry with an average diameter of ~105 nm and a core-shell structure. Compared with unmodified nanogels (fig. S2), the outer shells were continuous, and they were all about 6 nm thick, in accordance with that of the *E. coli* outer membranes (*45*). The confocal laser scanning microscopy (CLSM) image in fig. S4 shows a core-shell fluorescence structure, demonstrating the enclosure of nanogels in a fully covered *E. coli* membrane. The measurement of the surface charge of nanogels before and after the fusion of EM vesicles shows that the surface ζ potential changed from −7.9 ± 1.3 mV (nanogels) to −13.4 ± 0.7 mV (EM@nanogels), which is close to that of pure EM vesicles (−13.9 ± 1.3 mV) (Fig. 2B). Furthermore, the lipopolysaccharide (LPS) content of EM@nanogels measured by enzyme-linked immunosorbent assay immunoassay was about 17.4 mg liter^{-1}, which is close to that of pure EM vesicles (Fig. 2B).

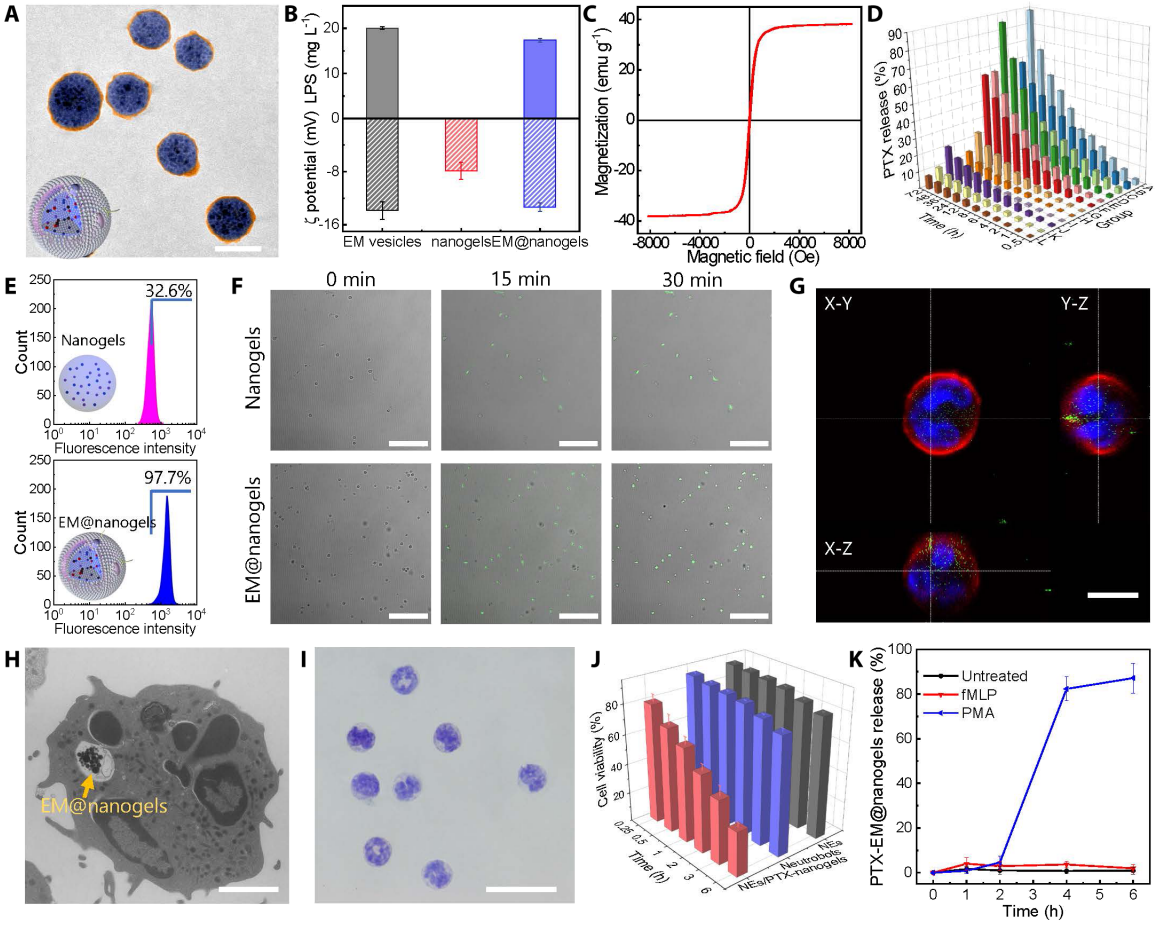

Fig. 2. Preparation and characterization of dual-responsive neutrobots. (**A**) Schematic and TEM images of EM@nanogels. Scale bar, 100 nm. Blue pseudo-color indicates nanogels, and orange pseudo-color indicates *E. coli* membrane. (**B**) LPS content of EM vesicles, nanogels, and EM@nanogels (top). ζ potential of EM vesicles, nanogels, and EM@nanogels (bottom) ($n = 5$; means ± SEM). (**C**) Magnetization (M) loop from SQUID analysis of EM@nanogels. (**D**) Cumulative release of PTX from EM@nanogels and nanogels at pH 5.0 and 7.4. Groups A to C: nanogels, pH 5.0, PTX added in preparation (1, 6, and 10 mg). Groups D to F: nanogels, pH 7.4, PTX added in preparation (1, 6, and 10 mg). Groups G to I: EM@nanogels, pH 5.0, PTX added in preparation (1, 6, and 10 mg). Groups J to L: EM@nanogels, pH 7.4, PTX added in preparation (1, 6, and 10 mg) ($n = 3$; means ± SEM). (**E**) Flow cytometry diagrams of the uptake of bare nanogels and EM@nanogels after incubation with NEs for 30 min. (**F**) Time-lapse CLSM images of NEs incubated with nanogels and EM@nanogels as a function of time. Scale bars, 100 μm. (**G**) 3D rebuilding CLSM image of a neutrobot. Scale bar, 5 μm. Nucleus of the neutrobot was labeled by Hoechst 33342 (blue). Cou6 (green)–loaded EM@nanogels were phagocytized by NEs to form neutrobots. Cell membranes of neutrobots were labeled by DiD (1,1′-dioctadecyl-3,3,3′,3′-tetramethylindodicarbocyanine perchlorate, red). EM@nanogels were shown with green fluorescence, and the cytomembranes of NEs were shown with red fluorescence, suggesting that EM@nanogels were mainly located inside NEs. (**H**) Schematic and TEM images of neutrobots. Scale bar, 2 μm. (**I**) Morphological images of neutrobots stained with Wright-Giemsa. Scale bar, 20 μm. (**J**) Viability of NEs, neutrobots, and NEs/PTX-nanogels as a function of time ($n = 3$; means ± SEM). (**K**) EM@nanogels release of neutrobots without treatment, neutrobots incubated with 10 nM fMLP, and neutrobots incubated with 100 nM PMA ($n = 3$; means ± SEM).

These results confirm a successful translocation of an *E. coli* membrane onto the outer surface of nanogels. Specifically, the magnetization of the as-prepared EM@nanogels was evaluated in a superconducting quantum interference device (SQUID) at 298 K. According to the magnetization curve, EM@nanogels displayed typical superparamagnetic behavior with the saturation magnetization (M_s) value of 38.2 emu g^{-1} (Fig. 2C). Although a small difference in temperature only has a minor effect on the magnetic property of EM@nanogels, it should be noted that the magnetization characterization by SQUID was carried out at 298 K rather than the physiological temperature (*46*). High-performance liquid chromatography was conducted to investigate the release kinetics of PTX from nanogels and EM@nanogels containing 1, 6, and 10 mg of PTX at pH 5.0 and 7.4. The release of PTX in nanogels at pH 7.4 increased from 3.5% at 1 hour to 9.8% at 4 hours and 85.4% at 72 hours, whereas the release at pH 5.0 was 7.0% at 1 hour, 16.1% at 4 hours, and 89.1% at 72 hours. By comparison, the PTX release in EM@nanogels at pH 7.4 went up from 1.7% at 1 hour to 3.7% at 4 hours and 20.8% at 72 hours and at pH 5.0 from 1.0% at 1 hour to 2.7% at 4 hours and 23.3% at 72 hours (Fig. 2D). The full coverage of *E. coli* membrane could prevent the leakage of PTX, which is of great importance for the viability of the as-prepared neutrobots.

For dual-responsive hybrid neutrobots, it is crucial that NEs phagocytize a maximal amount of EM@nanogels while the loaded EM@nanogels expose minimal toxicity to NEs. To evaluate the phagocytosis of EM@nanogels by NEs, equivalent amounts of alive *E. coli*, dead *E. coli*, EM@nanogels, and nanogels were tested in parallel (fig. S5). The degree of phagocytosis was quantified through

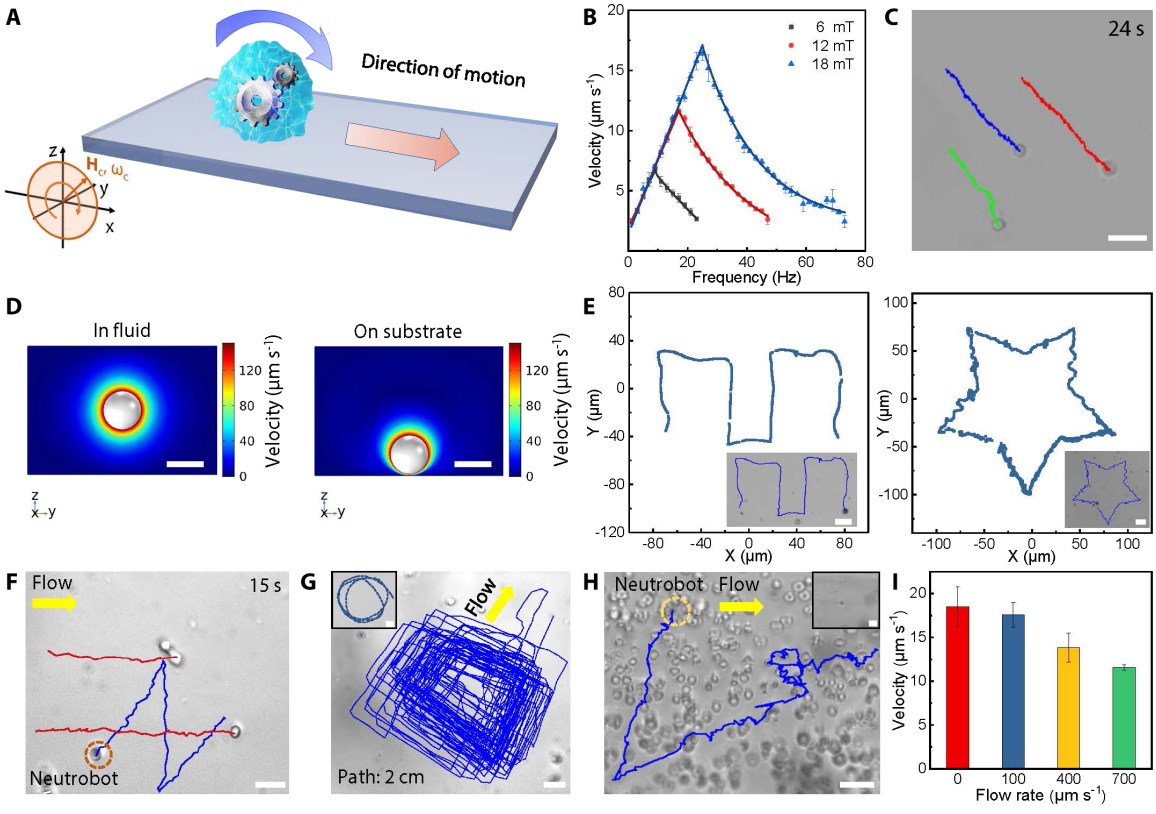

Fig. 3. Controllable magnetic actuation of neutrobot. (**A**) Schematic design of neutrobot motion under an RMF. (**B**) Velocity of neutrobots under RMF with different voltage and frequency ($n = 3$; means ± SEM). (**C**) Time-lapse image of three neutrobots under RMF (15 mT, 2 Hz). Scale bar, 20 μm. (**D**) Simulation of fluid flow near a neutrobot levitated in fluid and on substrate under magnetic field. Scale bars, 10 μm. (**E**) Time-lapse image and trajectories illustrating controllable magnetic propulsion of neutrobots in a predefined trajectory. Scale bars, 20 μm. (**F**) Time-lapse image showing magnetic propulsion of neutrobots have a *Z* trajectory against model blood flow (flow rate, 400 μm s^{-1}). Scale bar, 20 μm. (**G**) Time-lapse image showing long path of controllable magnetic propulsion against model blood flow over 1137 s. Scale bar, 20 μm. Inset image shows the relevant controllable magnetic propulsion in a circular track. Scale bar, 50 μm. (**H**) Time-lapse image exhibiting the controllable magnetic propulsion against blood flow. Inset image is the observed flow with focus on the center of the channel. Scale bars, 20 μm. (**I**) Velocities of magnetic propulsion of neutrobots against flow with different rates ($n = 3$; means ± SEM).

the measurement of the velocity of the migration of NEs. The speed of NEs in the EM@nanogel suspension was 0.08 μm s^{-1}, nearly six-fold faster than that in the nanogel suspension, which is comparable with that in the dead *E. coli* suspension. By using flow cytometry, we then evaluated the loading percentage of NEs that had been precultured with nanogels and EM@nanogels for 30 min (Fig. 2E). It was found that 97.7% of NEs engulfed EM@nanogels, which was notably higher than the percentage of NEs loaded with bare nanogels (32.6%). The average number of EM@nanogels loaded in each NE was estimated to be ~100 according to the change of EM@nanogel concentrations before and after phagocytosis. To better observe the phagocytosis of EM@nanogels by NEs, a green fluorescent dye, fluorescein isothiocyanate (FITC), was introduced to label EM@nanogels and nanogels. The time-lapse fluorescence microscopy images indicate that more EM@nanogels were taken up by NEs in 30 min in contrast with nanogels (Fig. 2F). The three-dimensional CLSM (3D CLSM) image of neutrobots shows that the EM@nanogels were mainly located inside the NEs (Fig. 2G). To clarify the subcellular distribution of EM@nanogels, ultrastructure analysis of neutrobots was carried out by using ultramicrotomy. After phagocytosis for 30 min, the ultrathin TEM section image shows a large aggregate with a diameter of ~1 μm in an intact phagosome membrane inside the cytoplasm (Fig. 2H). This aggregate should be made up by a number of the phagocytized EM@nanogels. The phagosome of EM@nanogels offered enough net magnetization to the neutrobot to enable magnetic navigation upon exposure to external RMF.

To evaluate the stability after phagocytosis, the morphology of neutrobots was examined by using the Wright-Giemsa stain. Similarly to the microscopic image of natural NEs (fig. S6), the morphology of neutrobots displayed a minor change after 30 min (Fig. 2I), demonstrating that the internalized EM@nanogels did not have a negative effect on the neutrobots. We further investigated the cell viability of NEs, PTX-loaded neutrobots, and NEs after engulfing PTX-loaded nanogels (NEs/PTX-nanogels) through the calcein-AM and propidium iodide (PI) double-staining method (Fig. 2J and fig. S7). Freshly isolated NEs and neutrobots showed cell viabilities of up to 81.1 and 78.3%, respectively, after being cultured for 6 hours, thus indicating a low cytotoxicity of EM@nanogels. By comparison, PTX-nanogel–loaded neutrobots (NEs/nanogels) had a cell viability of 29.7%, demonstrating that *E. coli* membrane cloaking substantially improved the biocompatibility of nanogels and also prevented the leakage of PTX from nanogels after 6 hours.

To investigate the release kinetics of EM@nanogels from neutrobots during different stages of active delivery—including magnetic propulsion in blood circulation (propulsion stage), chemotactic motion along the gradient of inflammatory factors (chemotaxis stage), and active target accumulation at inflammatory site (accumulation stage)—two model inflammatory factors, *N*-formyl-Met-Leu-Phe (fMLP) and phorbol myristate acetate (PMA), were used for the generated gradient of inflammatory factors in the chemotaxis stage and the triggered release of EM@nanogels in the accumulation stage, respectively. Figure 2K shows that the EM@nanogels from neutrobots in the untreated group (propulsion stage) released less than 2% in 6 hours, whereas the EM@nanogels in the presence of 10 nM fMLP (chemotaxis stage) had a slightly higher release of 4.0% in 6 hours. In the presence of 100 nM PMA, the neutrobots showed a low release of EM@nanogels after 2 hours (4.5%), which then markedly rose to 82.8% after 4 hours and finally slightly raised to 87.2% after 6 hours. Together, these results demonstrate that by sharing the biofunctions of the *E. coli* membrane, the EM@nanogels could elevate the efficiency of phagocytosis and prevent the release of PTX in the neutrobots. Our neutrobots can not only preserve good stability during the recruitment process but also rapidly release the PTX-loaded EM@nanogels triggered by the activating signals at the inflammatory site.

Controllable motion of magnetically actuated neutrobots

To propel our neutrobots, we used a vision-based magnetic navigation system consisting of an optical microscope for real-time visualization, a three-orthogonal Helmholtz coil pair system capable of generating a uniform magnetic intensity, and a closed-loop feedback module as a motion planner (fig. S8). By combining the capabilities of real-time position tracking, autonomous path planning, and vision-based feedback, our system enables self-navigation of neutrobots along a programmed path. Note that for a similar propulsion velocity, actuation by an RMF requires a lower amplitude than actuation by a gradient magnetic field to generate the same torque to yield a pulling force (*47*–*49*). Hence, RMF holds great promise for the clinical translation of neutrobots. Figure 3A shows a schematic illustration of the motion of magnetically actuated neutrobots on the polydimethylsiloxane (PDMS) substrate. Under actuation by an RMF, neutrobots with an asymmetric distribution of magnetic NPs could move with a rolling motion on the surface of a PDMS substrate, owing to the increase of apparent viscosity close to the surface, and the rolling direction of neutrobots should be identical to that of the circularly polarized RMF (H_c). The direction of motion of neutrobots was defined by the rolling motion of neutrobots with the PDMS substrate.

To examine the dynamics of neutrobots, the velocity of neutrobots was tested under actuation by RMFs with different intensities (6, 12, and 18 mT) and frequencies (1 to 75 Hz). At the low Reynolds number regime, the velocity increased almost linearly from 2.5 μm s^{-1} at 1 Hz to 6.9 μm s^{-1} at 9 Hz under the magnetic intensity of 6 mT (Fig. 3B). Once reaching the maximum synchronized frequency (step-out frequency) of 9 Hz, the velocity substantially declined as the frequency was increased. The change was caused by the fluidic drag beyond the maximal available magnetic torque, which led to the loss of synchronization between the neutrobot and RMF and thus the reduction of velocity. The magnetic torque by the uniform RMF could be strengthened by increasing the intensity of RMF. To improve the locomotion performance, the step-out frequency at 12 and 18 mT was increased to 17 and 25 Hz, respectively. Under a magnetic intensity of 18 mT and a frequency of 25 Hz, the neutrobots reached the maximum velocity of 16.4 μm s^{-1}, which is nearly 50-fold greater than the migration speed of natural NEs. In a control group, the bare nanogel-encapsulated neutrobots also facilitated magnetic propulsion (fig. S9) but exhibited a much slower step-out frequency (2 Hz) and velocity (5.2 μm s^{-1}) under the same parameters of RMF due to the small fraction of bare Fe_3O_4 NP–loaded nanogels engulfed by NEs as mentioned above.

We then investigated the kinematic characteristic of magnetically actuated neutrobots. The time-lapse image in Fig. 3C, captured from movie S2, illustrates that three neutrobots autonomously rolled on the PDMS surface along a given direction at a speed of 5.5 μm s^{-1} under an RMF of 15 mT and 2 Hz. In a control, the suspended neutrobots (green trajectory) caused efficient rotation under similar parameters of RMF but had negligible net displacement over time (fig. S10, captured from movie S3). To clarify the driving mechanism, the dynamics of magnetic propulsion were simulated by using a 2D fluid model. Supposing that NEs are spherical, the flow visualization displays a symmetric distribution around the neutrobot when the neutrobots are suspended in fluid (Fig. 3D). Note that even if the neutrobots close to the substrate exhibit asymmetric local flow along the vertical direction, the flow of fluid across the neutrobots in the horizontal direction is still symmetric. Therefore, the magnetic propulsion should be attributed to the fact that the RMF actuation on neutrobots leads to cell deformation (irregular) on the substrate, which could be verified from movie S2. The RMF-actuated deformation caused asymmetric local flow across neutrobots, which resulted in the aforementioned magnetic torque to propel the rolling motion of neutrobots. It should be noted that the resulting local asymmetric flow across neutrobots did not have direct contact with the substrate during the propulsion of neutrobots upon exposure to RMF (*50*). Furthermore, the direction of motion of neutrobots could be precisely navigated in real time through the manipulation of RMF. Two time-lapse trajectories in Fig. 3E illustrate that the neutrobots exhibited not only orthogonal turning with minor change of velocity but also a controllable pathway along a predetermined five-pointed star-shaped trajectory (captured from movie S4). Note that the neutrobots could be directly dragged with an average velocity of 0.9 μm s^{-1} upon exposure to a gradient magnetic field with an intensity of ~800 mT, but the RMF only needed a magnetic intensity of 6 mT to obtain a similar velocity (fig. S11 and movie S5).

Magnetically actuated navigation against the flow of blood is essential for the neutrobots to accomplish various tasks in the body. To investigate the magnetic motion of neutrobots against the direction of flow, a model of blood flow using a microfluidic filled with fresh blood was applied according to a previous report (fig. S12) (*51*). For flow with a rate of 400 μm s^{-1} (low erythrocyte density), Fig. 3F and corresponding movie S6A show that the neutrobots actuated by RMF (frequency of 5 Hz) displayed controllable motion (blue "*Z*" trajectory) against the flow with a velocity of 5.6 μm s^{-1}, whereas two natural erythrocytes used as references moved in the direction of flow (red linear trajectory). In addition, Fig. 3G illustrates the controlled movement of a neutrobot in the flow over the course of 1137 s, and the total traveling distance was estimated to be ~2 cm (movie S6B). The magnetically actuated neutrobots also facilitated long-distance unidirectional steerability in a circular track (inset in Fig. 3G). Furthermore, we examined the motion of magnetically actuated neutrobots against the blood flow with a rate

of ~700 μm s^{-1}, which is comparable to the velocity of physiological blood in microcirculation (*52*). The microscopic image in Fig. 3H, taken from movie S6C, displays a controllable "L" trajectory on the bottom of a model blood flow channel upon exposure to RMF (5 Hz). In contrast, the inset in Fig. 3H shows that the reference erythrocytes rapidly drifted with the flow at the middle layer of flow. Last, the velocities of neutrobots against the flow of fluid with different flow rates (0, 100, 400, and 700 μm s^{-1}) upon exposure to RMF were 18.5, 17.6, 13.8, and 11.6 μm s^{-1}, respectively (Fig. 3I). In summary, the neutrobots that had phagocytized magnetic EM@nanogels were capable of controllable locomotion in blood flow.

Collective motion of a swarm of neutrobots

To satisfy practical biomedical uses, it is critical to enable the collective motion control of neutrobots because this functionality provides a pathway to achieving sophisticated tasks and real-time visualization for spatiotemporal, resolution-limited imaging technologies in vivo. Because the magnetic rotation of neutrobots on the substrate causes local asymmetric flow, adjacent rolling neutrobots are expected to assemble into a swarm due to the interaction of their local flow (Fig. 4A). The time-lapse images in Fig. 4B, taken from movie S7, illustrate the interaction behavior of four neutrobots on the substrate upon an elliptically polarized RMF with a frequency of 15 Hz. One single rolling neutrobot moved close to the second neutrobot, and their pathway and movement behavior changed when the distance between them was ~1.5 μm, roughly corresponding to the range of their local flow field. The third and fourth neutrobots subsequently joined in, forming a dynamic chain swarm of neutrobots. Note that the tetra-neutrobot chain swarm was unstable once the RMF was turned off or the frequency dropped below 5 Hz, but the neutrobot chain swarm could be easily reconfigured by restarting the RMF.

The neutrobot swarm accelerated with the increasing frequency of RMF so long as it remained below the step-out frequency. Notably, the velocity of neutrobot chains increased with the number of neutrobots in the chain swarms (Fig. 4C). For example, the average velocity at 5 Hz of RMF elevated from 5.2 μm s^{-1} with one neutrobot to 24.9 μm s^{-1} with a tetra-neutrobot chain. Specifically, the average velocity of tetra-neutrobot chains at 15 Hz reached 53.5 μm s^{-1}, roughly fivefold faster than that of individuals (11.0 μm s^{-1}) at the same parameters of the RMF (Fig. 4D and movie S8). The formation frequency range of neutrobot swarms (1 to 15 Hz) is shown in fig. S13. To study the emergence of the neutrobot chain swarm, a computer simulation was carried out. The spatial trajectory of the neutrobots in the *Y*-*Z* plane indicates that each neutrobot experienced a "tank-treading" motion during the advancement of the chain (Fig. 4E). The fluctuation of the neutrobots on the *Y* axis rendered a positional exchange possible, and the hopping advancement along the *Y* axis reflected the movement of the chain.

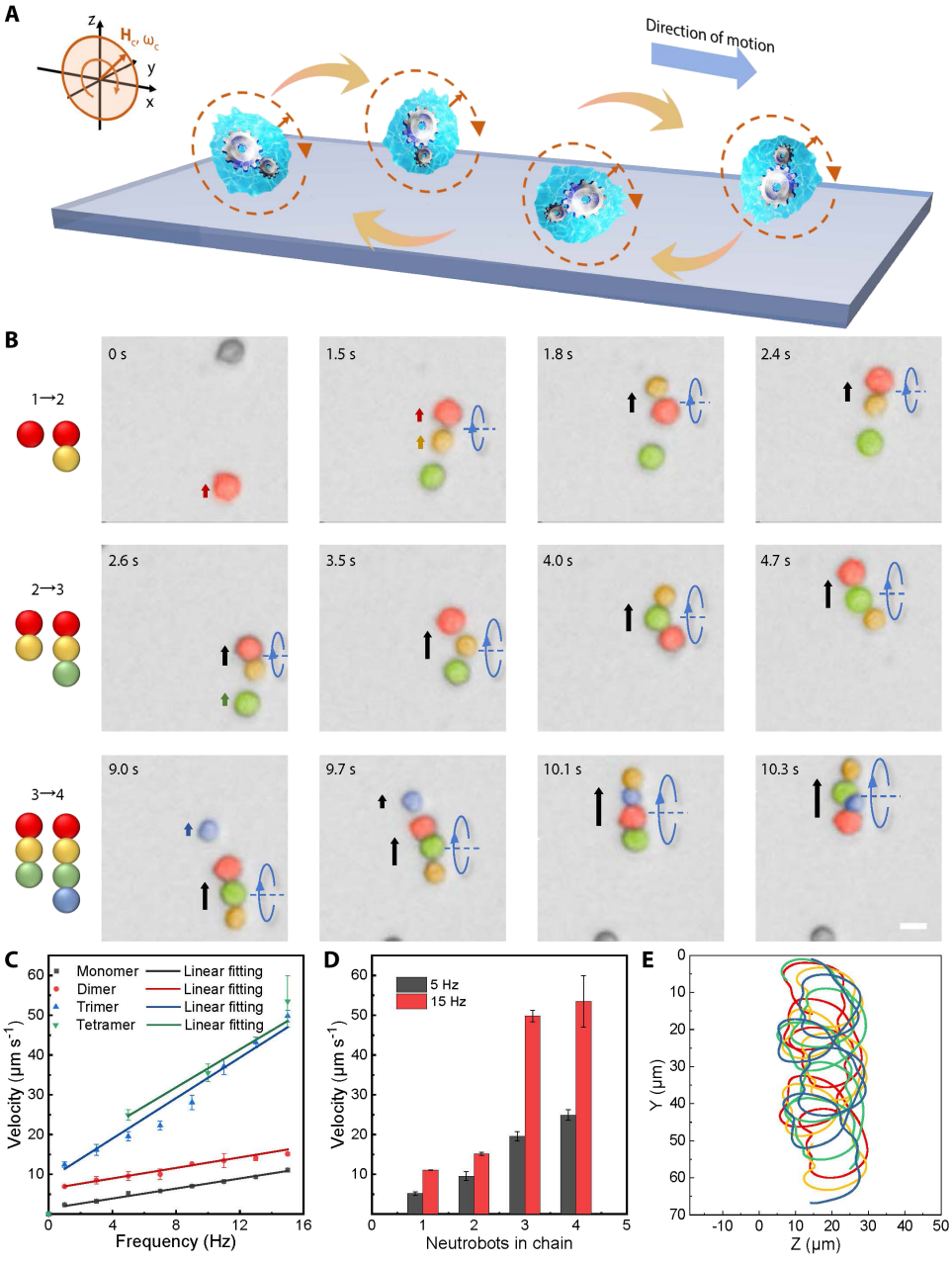

Fig. 4. Magnetic actuation of neutrobot swarm. (**A**) Schematic design of swarm formed by neutrobots under actuation by RMF. (**B**) Time-lapse images of the formation process from single neutrobot to tetra-neutrobot chain. Scale bar, 10 μm. (**C**) Dependence of neutrobot chain swarm on the frequency of the magnetic field ($n = 3$; means ± SEM). (**D**) Velocity profile of chains with different amounts of neutrobots. Intensity of magnetic field is 18 mT ($n = 3$; means ± SEM). (**E**) Simulation results of four neutrobots' trajectories in *Y*-*Z* plane.

The corresponding spatial position in the *Y*-*t* plane and *Z*-*t* plane during a locomotion cycle (fig. S14) shows the minor irregular trajectories in continuous motion circles, suggesting the stable motion of neutrobots during their collective rolling motion. The above experimental and theoretical analyses indicate that the neutrobots can assemble into a swarm upon the manipulation of RMF, and the swarm allows for considerably greater propulsion compared with a single neutrobot.

Chemotactic dynamics of neutrobots upon exposure to chemokine gradient

To realize the precise recognition of and active target delivery to inflammatory sites, we studied the chemotactic dynamics of neutrobots along a chemokine concentration gradient in a channel schematically shown in Fig. 5A. Here, a piece of agarose hydrogel containing 1 μM fMLP was used as a chemokine source to generate the chemokine gradient (CG). The time-lapse images of neutrobots in Fig. 5B, taken from movie S9, demonstrate that the neutrobots moved toward the hydrogel region containing 1 μM fMLP, indicating the chemotactic behavior of neutrobots.

To further study the dynamical behavior of neutrobots, the chemotactic motion of neutrobots in different concentration gradients of chemokines was evaluated with an Ibidi μ-Slide Chemotaxis^{3D} (fig. S15). Figure 5C shows the trajectories of neutrobots over 20 min (all normalized to a common origin) in a CG (10 pM μm^{-1}) formed by 10 nM fMLP solution added in one reservoir of μ-Slide. It can be seen that the neutrobots exhibited directional movement toward the direction of the higher chemokine concentration. The directional distribution of the chemotactic motion of neutrobots in Fig. 5D presents a centralized angle distribution in the range of −30° to +30° along a CG in this direction. These findings indicate that the neutrobots can autonomously sense the concentration gradient of chemokine and move toward the higher concentration region.

Furthermore, the dependence of the velocity of chemotactic motion of both NEs and neutrobots on the intensity of chemokine concentration gradients (Fig. 5E) was tested. The chemokine solution and fMLP-free medium were added to two separate reservoirs of the μ-Slide. The width of the channel between chemokine and medium was 1 mm. The chemokine concentration gradient was formed across the channel (fig. S15). The chemotactic velocity of both NEs and neutrobots went up with the intensity of chemokine concentration gradient and had a maximum velocity of 0.21 μm s^{-1} in a CG formed by 100 pM μm^{-1}. Note that the velocity of neutrobots was commensurate with that of normal NEs under the same conditions and comparable with that of activated NEs with *E. coli*. To evaluate the effect of magnetic functionalization on the motility of NEs, the velocities of NEs and neutrobots under the CG were compared. As shown in Fig. 5E, no substantial difference

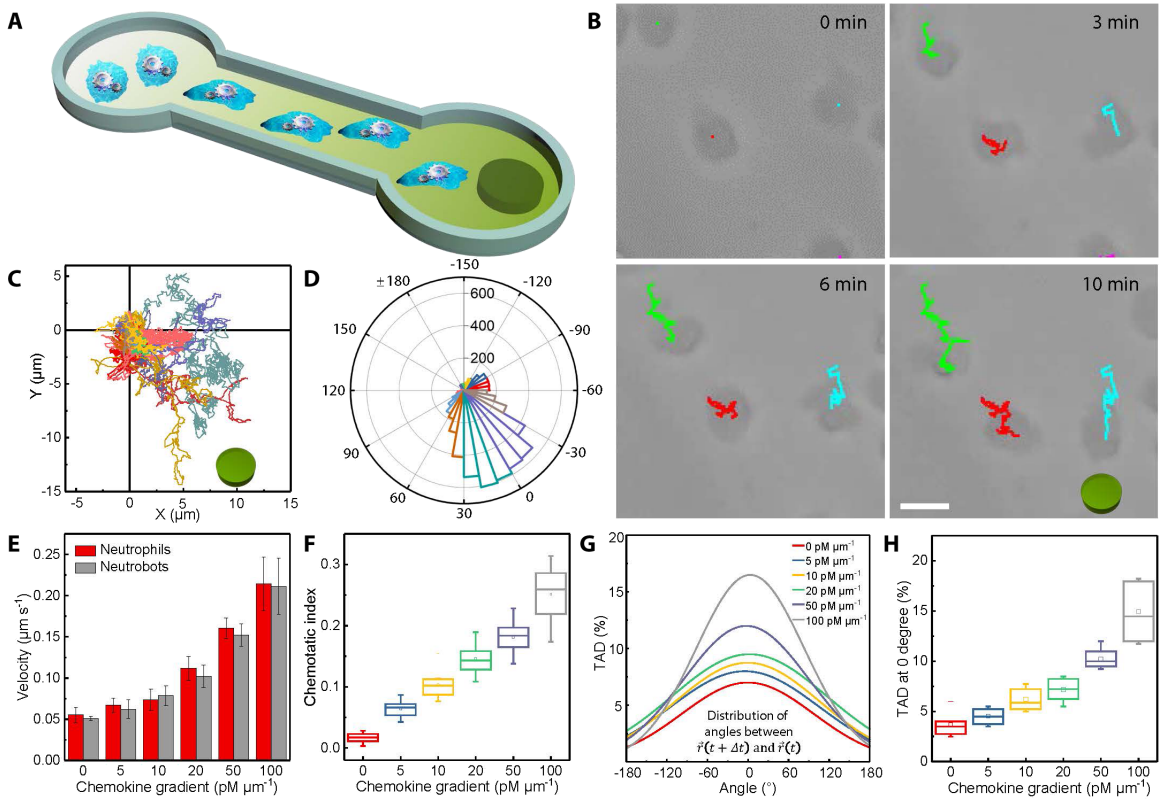

Fig. 5. Chemotactic dynamics of neutrobots upon CG. (**A**) Schematic of chemotactic motion of neutrobots along the gradient of chemokine. To model a CG, fMLP (green color) was loaded into agarose hydrogel, and the resulting hydrogel was placed in solution to create a CG. (**B**) Time-lapse images illustrating the chemotactic motion of neutrobots along a CG from an agarose gel with 1 μM fMLP. Scale bar, 10 μm. (**C**) Trajectories ($n > 80$) and (**D**) direction distribution ($n > 5000$) of neutrobots upon a gradient of fMLP (10 pM μm^{-1}). Duration of chemotactic motion is 20 min. (**E**) Dependence of chemotaxis velocity of NEs and neutrobots on the gradient of fMLP ($n = 5$; means ± SEM). (**F**) Dependence of CI (ratio of distance to path length) of neutrobots on the gradient of fMLP ($n = 10$; means ± SEM). (**G**) TAD of neutrobots under CG ($n = 600$). (**H**) TAD at 0° of neutrobots under different gradients of fMLP ($n = 7$; means ± SEM).

in chemotactic velocity was found between the NEs and neutrobots, suggesting that the uptake of magnetic EM@nanogels did not affect the chemotaxis ability of neutrobots. Meanwhile, we estimated the migration persistence on the basis of the chemotactic index (CI), which represents the ratio of the total displacement to the length of the path. As shown in Fig. 5F, the CI of neutrobots is also related to the fMLP concentration. To quantify the distribution of orientation of the neutrobots with respect to the chemokine concentration gradient, we examined the turning angle distribution (TAD) (*53*), which is defined as the distribution of angle between two adjacent displacements during the chemotactic motion (fig. S16). As the neutrobots started to exhibit self-propulsion and positive chemotaxis, the distribution of neutrobots was polarized toward the direction of the gradient (Fig. 5G). In contrast, the neutrobots had an equal distribution of turning angle in the absence of chemokine. Moreover, a more condensed distribution of turning angle appeared with higher chemokine concentration (Fig. 5H). The curve of TAD at 0° versus chemokine concentration shows a typical ballistic behavior with a chemotactic response toward the CG. Note that the chemotactic behavior of neutrobots displayed negligible differences with that of natural NEs (fig. S17). These results suggest that a higher chemokine concentration gradient causes a more intense response of neutrobots, and thus, the velocity of neutrobots may be modulated through the intensity of chemokine concentration gradients.

Dual-responsive dynamics of neutrobots ex vivo

It is of great importance for the dual-responsive neutrobots to accomplish effective movement in real blood vessels as schematically illustrated in Fig. 6A. To this end, a section of blood vessel was freshly dissected from the aorta of a rat (the inset photo in Fig. 6A), and the motion of neutrobots was observed in the blood vessel. The dual-responsive motion process of neutrobots is shown in Fig. 6B and movie S10. The neutrobots were added into the blood vessel, which was placed in an RMF. A drop of chemokine solution was injected into the dissected blood vessel to model the inflammatory site. First, the neutrobots rolled to the chemokine source during 0 to 40 s, indicated by the red trajectories (under an RMF of 15 mT and 2 Hz). After that, the RMF was turned off and the neutrobots began a continuous chemotactic movement shown by blue trajectories along the chemokine concentration gradient until 200 s. The dual-responsive movement shows that after the magnetic propulsion, the neutrobots still had autonomous chemotactic capability. The velocity and direction distribution of neutrobots during magnetic propulsion and chemotactic motion were further analyzed. The trajectories of dual-responsive neutrobots in Fig. 6C, drawn from Fig. 6B, show that the neutrobots had similar trajectories when driven by RMF, but notable differences were found in their chemotactic trajectories. Note that the histogram in fig. S18 illustrating the dynamic velocity on the surface of PDMS exhibits a narrower distribution upon exposure

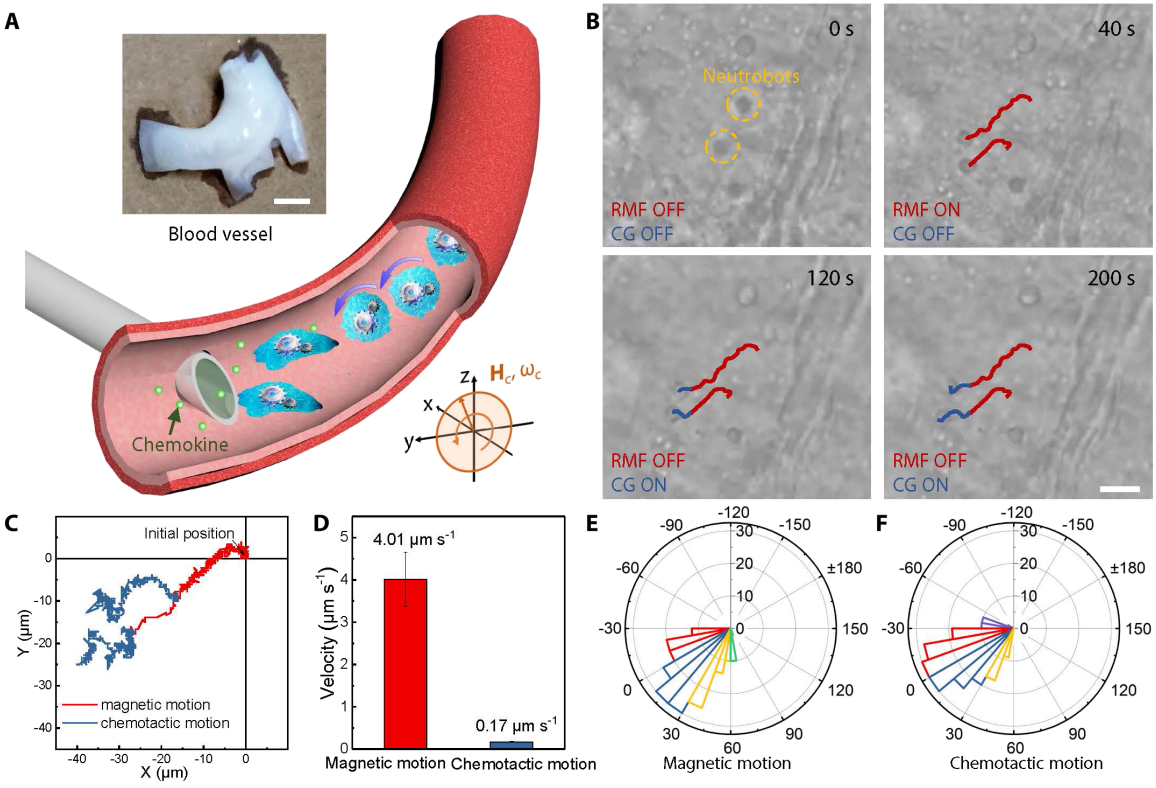

Fig. 6. Dual-responsive intravascular movement of neutrobots. (**A**) Schematic of dual-responsive motion of neutrobots under external RMF toward the source of chemokine on blood vessel. Injection of chemokine is used to establish CG. The inset photograph is the actual blood vessel in the experiment. Scale bar, 2 mm. (**B**) Time-lapse images illustrating the movement of dual-responsive neutrobots in a blood vessel. The red lines represent the trajectories of neutrobots under magnetic field, and the blue lines represent the trajectories of neutrobots under the gradient of chemokine. Scale bar, 20 μm. (**C**) The flexural trajectories of magnetic motion (red lines) and chemotactic motion (blue lines) of neutrobots. The neutrobots were controlled to perform magnetic motion for 40 s and chemotactic motion for 160 s. (**D**) Average velocities of neutrobots during magnetic motion and chemotactic motion ($n = 3$; means ± SEM). (**E** and **F**) The direction distributions of neutrobots during (E) the magnetic motion ($n > 150$) and (***F***) the chemotactic motion ($n > 150$).

to RMF with a frequency of 2 Hz, ranging from 4 to 8 μm s^{-1}. In contrast, the dynamic velocity on the surface of vessels ranged from 2 to 7 μm s^{-1}. The average velocity on PDMS was 5.2 μm s^{-1}, slightly higher than that on the vessel (4 to 8 μm s^{-1}), suggesting that the surface roughness of the substrate influences the magnetic propulsion (*27*). In addition, Fig. 6D shows that the magnetically driven motion of neutrobots in an RMF at 15 mT and 2 Hz had an average velocity of 4.0 μm s^{-1}, substantially higher than the average velocity of chemotactic motion, 0.17 μm s^{-1}. To confirm the directional motion of both the magnetic actuation and chemotaxis, their direction distributions (Fig. 6, E and F) were calculated. Figure 6E shows that the direction of magnetically driven motion had a narrow distribution, owing to its good controllability. Similarly, Fig. 6F reveals the similar direction distribution of chemotactic motion and magnetic propulsion, suggesting the active target capability of dual-responsive neutrobots to the region of higher chemokine concentration (i.e., inflammatory site). Overall, the data in Fig. 6 indicate that the neutrobots in blood vessels are capable of both propulsion upon exposure to RMF and chemotactic motion in response to a gradient of inflammatory factors. Therefore, these neutrobots offer a platform for active therapy in vivo.

Actively penetrating the BBB

A model BBB with glioma tumor cells inside the barrier was established on the basis of a porous Transwell system containing a μ-Slide membrane flow microchannel (fig. S19). The penetration of neutrobots across the model BBB and the subsequent release of EM@nanogels triggered by PMA in the porous Transwell system are schematically illustrated in Fig. 7A. A monolayer of bEnd.3 cells was seeded on the 3-μm porous Transwell membrane as the model BBB (*54*). The differential interference contrast (DIC) microscopy image in Fig. 7A (top right) suggests a tight cell junction and no apparent

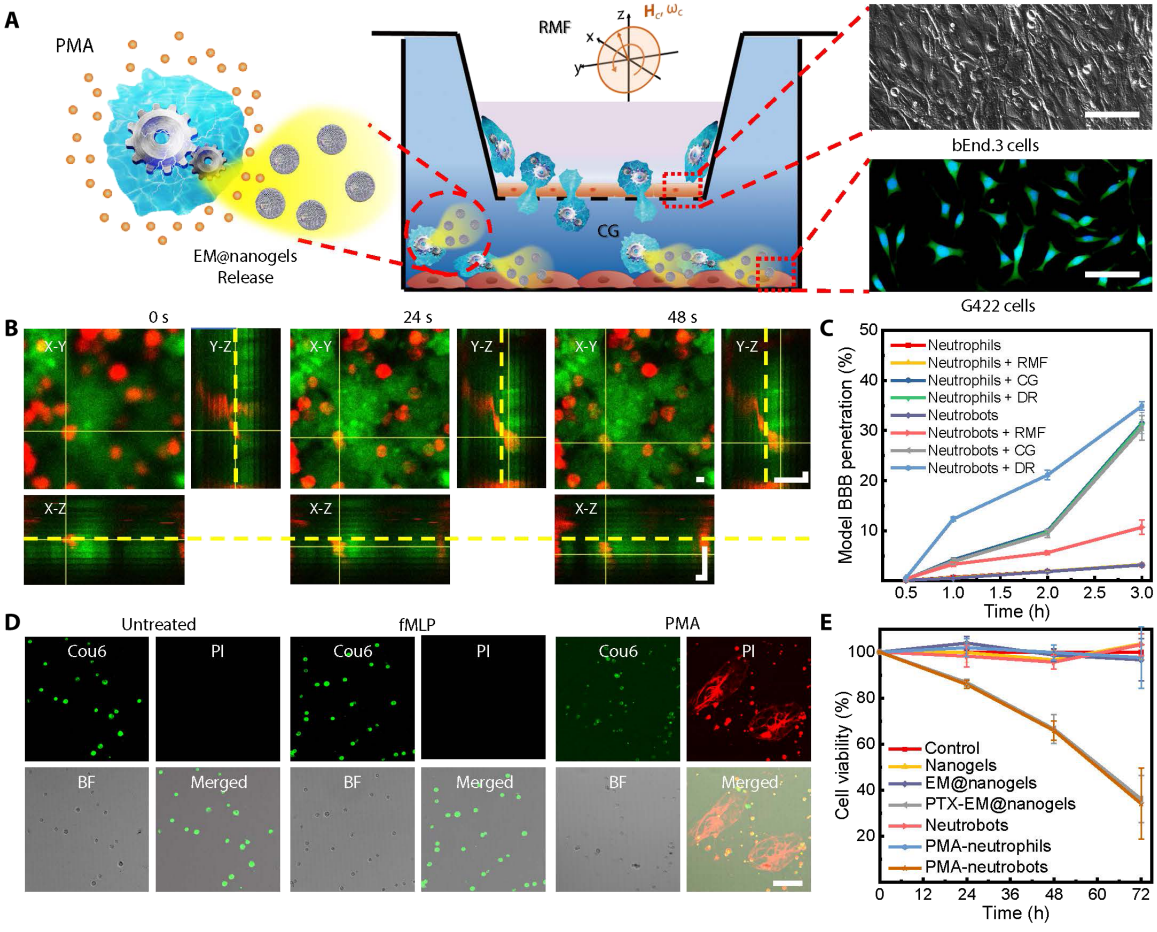

Fig. 7. Active delivery of neutrobots to glioma cells in vitro. (**A**) Schematic of the evaluation of neutrobots to penetrate BBB and release drug toward glioma cells by using a Transwell-based system. To establish the system, a layer of mouse cells (bEnd.3) grown on a polycarbonate (*58*) membrane served as the BBB, and G422 cells (a kind of glioma cell) were cultivated at the bottom of the Transwell. The neutrobots can penetrate the BBB and release EM@nanogels to G422 cells upon PMA. The fluorescence microscope images illustrate calcein-AM– and Hoechst 33342–labeled G422 cells, and the DIC image shows bEnd.3 cells in the system. Scale bars, 75 μm. (**B**) Time-lapse CLSM images showing the penetration of neutrobots across model BBB. In the images, bEnd.3 cells were labeled by calcein-AM and neutrobots were labeled by DiI. The yellow dashed lines indicate the starting depth of the neutrobot. Scale bars, 4 μm. (**C**) Penetration ratio of NEs or neutrobots to model BBB under various conditions. Concentration of fMLP in the lower chamber is 10 nM ($n = 3$; means ± SEM). (**D**) CLSM images showing drug release of neutrobots under different conditions after being cultured for 6 hours. Untreated neutrobots (left), 10 nM fMLP-treated neutrobots (middle), and 100 nM PMA-treated neutrobots were tested. EM@nanogels were loaded with Cou6, and the released DNA segments were stained with PI. Scale bar, 100 μm. (**E**) Cytotoxicity of nanogels, EM@nanogels, PTX-loaded EM@nanogels, neutrobots, PMA-treated NEs, and PMA-treated neutrobots against G422 cells for different times ($n = 5$; means ± SEM).

gap among cells, demonstrating that bEnd.3 cells were successfully grown on the porous membrane of the Transwell system. Because the nuclei were labeled by Hoechst 33342 and calcein-AM was used as a fluorescence viability indicator, the CLSM image of G422 cells in the lower chamber (Fig. 7A, bottom right) shows the emergence of green fluorescence in the calcein-AM channel, verifying the viability of cancer cells. The lower chamber was filled with fetal blood serum (FBS)–free medium with 10 nM fMLP to form a gradient near the model BBB and 100 nM PMA to simulate the condensed inflammatory factors at the diseased site (*55*). After the neutrobots were added to the upper chamber, under the guidance of RMF and CG, the neutrobots actively moved toward and crossed the model BBB, reached the infectious site, and released the drug-loaded nanogels triggered by PMA (Fig. 7A, middle and left).

To observe the fluorescence image, the bEnd.3 cells were labeled with calcein-AM, and the neutrobots were labeled with 1,1′-dioctadecyl-3,3,3′,3′-tetramethylindocarbocyanine perchlorate (DiI). The dual-responsive neutrobots first rolled on the surface of the bEnd.3 cell layer of the porous membrane toward the model diseased site. The fMLP was then added to the bottom chamber, creating a CG through the porous membrane, which triggered the chemotaxis of dual-responsive neutrobots across the model BBB. Time-lapse 3D CLSM top-view (*X*-*Y* plane) images in Fig. 7B, captured from movie S11, show that the dual-responsive neutrobots had minor displacement within 48 s while the size of neutrobots gradually became smaller. The corresponding time-lapse images in the *Y*-*Z* and *X*-*Z* planes indicate that the neutrobots migrated along the gradient of fMLP and crossed the bEnd.3 cell layer on the porous membrane. Last, a large number of dual-responsive neutrobots were observed at the bottom of the chamber.

Furthermore, an investigation on the active BBB penetration of dual-responsive neutrobots in vitro was carried out for 3 hours, but the magnetic actuation of an AC RMF with an intensity of 15 mT and a frequency of 2 Hz was only conducted for 1 hour as illustrated in fig. S20. The percentage of DR neutrobots that crossed the model BBB as a function of time was quantified by calculating the number of neutrobots observed at the bottom of the chamber. Equivalent amounts of neutrobots and NEs, neutrobots and NEs upon exposure to RMF, neutrobots and NEs upon exposure to CG, and NEs upon exposure to both RMF and CG (i.e., DR) were also tested in parallel as controls. As shown in Fig. 7C, percentages of neutrobots and NEs, which served as controls, periodically increased and reached 3.2% at 3 hours, indicating that gravity played a minor role in the performance of BBB penetration. As expected, RMF played a negligible role in the enhancement of NEs. In contrast, the percentage of neutrobots was elevated to 10.7% upon exposure to RMF for 3 hours, which may be attributed to the accelerated accumulation of magnetically propelled neutrobots on the model BBB. Moreover, similar to NEs upon exposure to CG, the percentage of neutrobots upon exposure to CG slowly increased to 9.5% in model BBB penetration within the first 2 hours and considerably increased by 21% within 2 to 3 hours. The data on CG exposure suggest that limited neutrobots and NEs arrived on the model BBB in the first 2 hours. Subsequently, a high number of neutrobots and NEs diffused onto the model BBB and efficiently penetrated the model through chemotactic motion. Among the various treatments, dual-responsive neutrobots displayed a nearly linear increase every hour; the corresponding results were 12.4% at 1 hour, 21.1% at 2 hours, and 34.9% at 3 hours. Because of the combination of accelerated arrival to the model BBB cell sheet through magnetic propulsion and chemotactic motion along the gradient inflammatory factor, dual-responsive neutrobots achieved efficient penetration of the model BBB, with which natural NEs and synthetic swimming microrobots could not compare.

After penetrating the BBB, the therapeutic effect of dual-responsive neutrobots on cancer cells in vitro was examined. EM@nanogels were stained with a fluorescence dye, coumarin 6 (Cou6), and PI was used as an indicator of NETs. The CLSM images in Fig. 7D show that the green fluorescence dots in the Cou6 channel overlapped with the bright-field image of neutrobots, suggesting that the Cou6-lableled EM@nanogels were still encapsulated inside the neutrobots of both the untreated and fMLP groups after 6 hours. In the presence of 100 nM PMA, however, the intensity of green fluorescence dots in the PMA group weakened, and, accordingly, the green fluorescence covered the whole field of vision in the Cou6 channel. Specifically, the strong red fluorescence in the PI channel shows the wide distribution across the neutrobots, suggesting the disruption of their plasma membranes along with the formation of NETs. In a control experiment, Cou6-EM@nanogels from the untreated, fMLP, and PMA groups were located inside neutrobots at 0 hours (fig. S21). To further examine the uptake of the released EM@nanogels by tumor cells, both the untreated and PMA-treated neutrobots were incubated with G422 cells (a model glioma cell). The intensity of green fluorescence dots in Cou6-EM@nanogel–loaded neutrobots disappeared, whereas the green fluorescence of G422 cells appeared (fig. S22), meaning that Cou6-EM@nanogels were taken up by G422 cells. The therapeutic effect of neutrobots was further quantitatively estimated by the measurement of the viability of G422 cells with different treatments, including drug-free nanogels, drug-free EM@nanogels, PTX-loaded EM@nanogels, untreated neutrobots with PTX-loaded EM@nanogels, PMA-treated NEs, and PMA-treated neutrobots with PTX-loaded EM@nanogels (Fig. 7E). Note that neutrobots and NEs were pretreated with 100 nM PMA for 4 hours before the treatment of G422 cells. In contrast to the negligible effect of other samples on the viability of G422 cells, both the PMA-treated neutrobots and PTX-loaded EM@nanogels led to a ~65% reduction of G422 cell viability. The above data in vitro illustrate that the neutrobots can not only maintain the encapsulated drug during chemotactic motion but can also efficiently release the drug for active therapy to cancer cells.

Active drug delivery to postoperative glioma in vivo

After having characterized the BBB penetration of dual-responsive neutrobots in vitro, we further investigated their active target delivery to a model postoperative glioma in vivo. To this end, a postoperative glioma model was constructed. Briefly, the mice were first inoculated with 2 μl of G422 cells by intracranial injection. After 10 days, CLSM images in fig. S23 confirm the successful inoculation of gliomas inside the brains of mice. Next, a small part of gliomas of half of the glioma-bearing nude mice were surgically resected. Subsequently, all of the glioma-bearing mice were separated into four groups, namely, neutrobots-injected mice without surgery operation and RMF treatment (control group), neutrobots-injected mice with RMF operation and no surgery treatment (RMF group), neutrobots-injected mice with surgery treatment and no RMF operation (CG group), and neutrobots-injected mice with surgery treatment and RMF operation (DR group) (Fig. 8A). Note that the in vivo RMF operation was performed by a homemade setup (fig. S24) and only

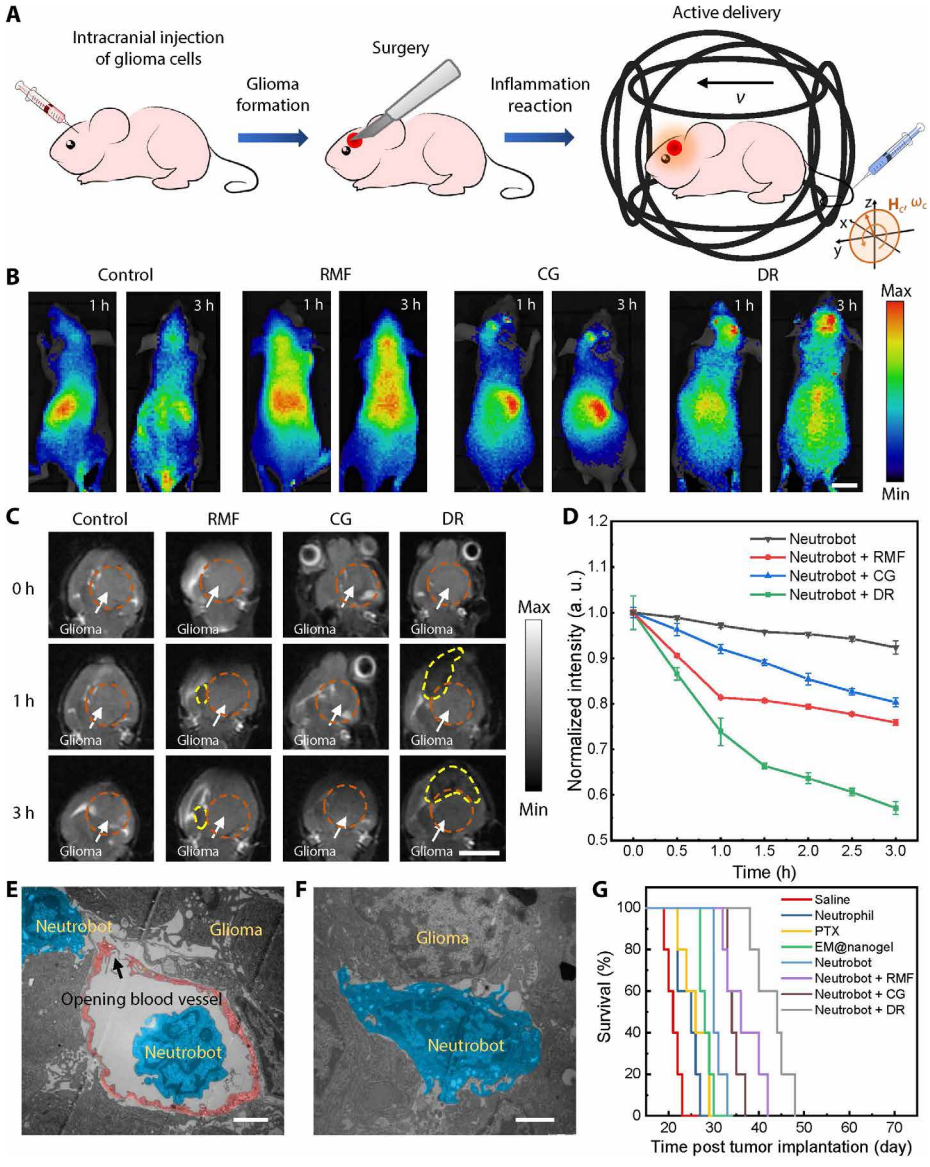

Fig. 8. Active delivery of neutrobots to postoperative glioma. (**A**) Schematic diagram of the glioma surgical resection model and active accumulation of neutrobots to inflamed postoperative glioma through magnetic propulsion and chemotaxis. (**B**) In vivo fluorescence images of glioma-bearing mice (control group), glioma-bearing mice after surgical treatment (CG group), glioma-bearing mice treated with RMF (5 mT, 1 Hz) for 1 hour (RMF group), and glioma-bearing mice after surgical treatment and treated with magnetic field for 1 hour [dual response group (DR group)]. Neutrobots were labeled by 1,1′-dioctadecyl-3,3,3′,3′-tetramethylindotricarbocyanine iodide (*21*). Scale bar, 10 mm. (**C**) In vivo T_2-weighted MR imaging of glioma (G)–bearing mice after injection of neutrobots, where 3×10^6 neutrobots were intravenously injected into each mouse. Time for RMF treatment was 1 hour. CG was formed through partial surgical resection of glioma. Scale bar, 10 mm. (**D**) Normalized intensity of signal in the glioma (G) area in glioma-bearing mice after injection of neutrobots and different treatments ($n = 3$; means ± SEM). (**E**) TEM image of neutrobots located in the blood vessel and outside the blood vessel. This tissue was taken from the glioma of the glioma-bearing mouse in the group of neutrobots with dual-response treatment (neutrobots + DR) 3 hours after injection of neutrobots. Red pseudo-color represents the blood vessel, and blue pseudo-color represents neutrobots. Scale bar, 2 μm. (**F**) TEM image of neutrobots located in the glioma tissue, where blue pseudo-color represents neutrobots. Scale bar, 2 μm. (**G**) Survival curves of glioma-bearing mice with various therapies. Saline was injected into glioma-bearing mice to form the negative control group. NEs, PTX solution, and EM@nanogels were injected into postoperative glioma-bearing mice. Neutrobots were injected into glioma-bearing mice to form the neutrobots group. Neutrobots were injected into glioma-bearing mice that were then treated by RMF to form the neutrobots with RMF treatment group (neutrobots + RMF group). Neutrobots were injected into postoperative glioma-bearing mice to form the neutrobots with CG treatment group (neutrobots + CG group). Neutrobots were injected into postoperative glioma-bearing mice that were then treated by RMF for 1 hour to form the neutrobots + DR group ($n = 5$).

proceeded for 1 hour. To observe the distribution of dual-responsive neutrobots in the mice with an in vivo fluorescence imaging system (IVIS Lumina III, PerkinElmer Inc.), 1,1′-dioctadecyl-3,3,3′,3′-tetramethylindotricarbocyanine iodide (*21*), a near-infrared fluorescent, was incorporated into the neutrobots. As shown in Fig. 8B, the fluorescence in the control group appeared throughout almost the whole body, but the fluorescence intensity in the brain was very low at 1 and 3 hours. In the RMF group, the fluorescence intensity in the brain slightly increased compared with that of the control group. Similar with the RMF group, the fluorescence in the CG group showed a higher fluorescence signal in the brain compared with the control group. Notably, the fluorescence signal of the brain in the DR group was apparently higher than those of other groups. In addition, the fluorescence quantitative analysis on the harvested organs of the aforementioned mice shows that the accumulation of neutrobots in the brain in the control group, RMF group, CG group, and DR group were 3.6, 9.8, 4.3, and 11.4%, respectively (fig. S25).

Next, a T_2-weighted magnetic resonance imaging (MRI) system was used to better visualize the glioma in the brains of mice in the above four groups owing to the limited tissue penetration of the in vivo fluorescence imaging system. To this end, we first tested the T_2 signal intensity of neutrobots, magnetic particles, and blood. Figure S26 shows that the blood had a very low MRI signal, whereas the neutrobots exhibited similar MRI intensity with the magnetic particles (0.025 mg ml^{-1}), suggesting that dual-responsive neutrobots could be imaged by the MRI system. The in vivo MRI images of glioma-bearing mice in Fig. 8C show that, in contrast with the gray value and area of the indicated yellow region in the brains of the control group, RMF group, and CG group, the gray value notably decreased and the gray area increased for the DR group, which indicates that many neutrobots accumulated around the glioma. Moreover, the normalized gray intensity of the indicated orange region of gliomas in the four groups decreased, signaling the arrival of neutrobots in the glioma (Fig. 8D). Notably, the gray value in the glioma of the control group decreased ~7% in

3 hours, meaning that the weak gradient of inflammatory factors caused by the glioma could also guide the chemotactic motion of a small amount of neutrobots toward the glioma. The gray value in the glioma of the CG group decreased by 20% in 3 hours because of the stronger gradient of inflammatory factors generated by the surgical treatment. In addition, the gray value of glioma in the RMF group rapidly decreased by ~19% in 1 hour because the RMF operation was only sustained for 1 hour. Notably, the gray value in the DR group had a similar decreasing tendency with that of the CG group in 3 hours, but it had a roughly sixfold reduction (~43%) compared with the control group. Together with the data of in vivo fluorescence photographs and MRI images, the dual-responsive neutrobots exhibited the highest brain-targeting efficiency in the brain of the glioma-bearing mice in all of the model groups, verifying that the higher accumulation of PTX in the brain of the glioma-bearing mice resulted from the higher presence of neutrobots after the RMF operation for 1 hour and chemotactic motion.

Further examination of the ultrathin section of the gliomas in the DR group at 3 hours was performed. The TEM histological section images of the blood vessels of gliomas show that one neutrobot, preserving its intrinsic shape, was located on one side of the vessel wall of the glioma (Fig. 8E). An evident opening on the vessel wall could be observed, where another neutrobot with a compressed geometry was visible close to the opening. We posit that the neutrobots in the blood vessels entered the glioma by penetrating across the BBB. In addition, the TEM images of the histological sections of the brains in Fig. 8F and fig. S27 demonstrate the permeation of dual-responsive neutrobots into the glioma tissues from the vessel. Furthermore, the observed number of neutrobots in the glioma from the histological sections of the DR group was about 2.5-fold greater than that of the control group (fig. S28), suggesting the efficient delivery of dual-responsive neutrobots.

Last, the therapeutic efficacy of dual-responsive neutrobots against the glioma was evaluated by recording the survival time of glioma-bearing mice (Fig. 8G). Here, eight groups of glioma-bearing mice were intravenously injected with equivalent amounts of saline (saline group), NEs (NE group), PTX solution (PTX group), PTX-loaded EM@nanogels (EM@nanogel group), PTX-loaded neutrobots (neutrobot group), PTX-loaded neutrobots upon exposure to RMF (neutrobot + RMF group), PTX-loaded neutrobots upon exposure to CG (neutrobot + CG group), and dual-responsive PTX-loaded neutrobots (neutrobot + DR group). Note that the brain gliomas of the saline, NE, PTX, EM@nanogels, neutrobot + CG, and neutrobot + DR groups were treated surgically. The median survival times for the saline, NE, PTX, EM@nanogel, neutrobot, neutrobot + RMF, neutrobot + CG, and neutrobot + DR groups were 20, 22, 25, 27, 30, 35, 33, and 43 days, respectively. Notably, the tumor-associated inflammatory response was amplified after surgical treatment, which resulted in the enhanced chemotactic capacity of the neutrobots to target the infiltrating glioma cells. In addition, the body weight of glioma-bearing mice in the neutrobot + DR group exhibited the highest stability, as shown in fig. S29. These data indicate that both the RMF operation and surgical treatment improved the accumulation of PTX-loaded neutrobots at the glioma sites, so the dual-responsive neutrobots could actively deliver the greatest number of PTX-loaded nanogels to the diseased region. In addition, there were no noticeable signs of neurodegeneration—such as tremor, balance problems, or decreased movement behavior—throughout the treatment of the glioma-bearing mice. Meanwhile, the biosafety of dual-responsive neutrobots for active target delivery was further evaluated by hematoxylin and eosin (H&E) pathological staining assay. The major organs were harvested from the glioma-bearing mice of the above-mentioned eight models for H&E staining analysis. In contrast with the saline group, no pathological abnormalities or inflamed cells in the brain, heart, liver, spleen, lung, or kidney in the treated model groups were observed, demonstrating the negligible toxicity of neutrobots on the mice (fig. S30).

DISCUSSION

Three major challenges should be overcome for using cell-based swimming microrobots to realize active target delivery. First, both biocompatibility and biodegradability are essential for the prolonged lifetime of cell-based swimming microrobots in the body. Sperm- and bacteria-hybrid swimming microrobots, for example, suffer from immune attack after entry into the bloodstream. Second, the efficient encapsulation of therapeutic agents is crucial for the viability of cell-based microrobots to accomplish their tasks. Third, penetration across various biological barriers, such as the BBB, to inflamed or pathogenic areas is of great importance for active target delivery. To address these issues, we demonstrate a dual-responsive NE-based microrobotic system through active phagocytosis of EM@nanogels and drug-loaded magnetic nanogels by natural NEs. The resulting neutrobots preserve the intact membrane structure and immunosuppressive antigens of natural NEs such as CD47. They can evade attacks from the immune system through their interaction with various inhibitory receptors such as signal regulatory protein α (*56*), resulting in a prolonged lifetime in the circulatory systems. Furthermore, *E. coli* membrane cloaking enables the high loading capacity of nanogels by NEs and the reduction of drug leakage. The highly loaded magnetic particles inside the neutrobots enable a net magnetic alignment upon exposure to a programmable RMF and subsequently allow the controllable motion of individual neutrobots and swarms of neutrobots. Inheriting the chemotaxis of natural NEs, the chemotactic motion of neutrobots along the gradient inflammatory factors allows the neutrobots to travel to the inflamed site and penetrate across the BBB. In vivo experiments verify the active target delivery of dual-responsive neutrobots to the glioma.

Our investigations represent a conceptual design of dual-responsive neutrobots that couples the controllable propulsion function of magnetically actuated swimming microrobots with the biological feature of natural NEs for active target delivery. Active target delivery of dual-responsive neutrobots in vivo has been verified by using a partially postsurgical model of the glioma-bearing mouse. The purpose of surgical operation is to amplify the concentration of inflammatory factors, and the MRI data illustrate a minor effect on the integrity of the glioma tissues. Further quantification analysis shows that the delivery efficiency of the neutrobot group without RMF treatment and surgical operation is much lower than that of the dual-responsive neutrobot group, suggesting that the BBB still has a substantial influence on the penetration of neutrobots. In addition, dual-responsive neutrobots exhibit good delivery efficiency to the glioma-bearing mice without surgical operation, proving that the active target delivery by using dual-responsive neutrobots can be used without surgical operation because glioma causes local inflammation (*57*).

Programmable locomotion along a predetermined path (e.g., five-pointed star-shaped trajectory) by coupling the RMF system

with vision-based real-time feedback in vitro has been demonstrated. However, the current imaging platform is unable to perform the task of real-time feedback of both the position of neutrobots and the optical route to the diseased site in vivo, owing to the limitation of spatiotemporal resolution and depth-to-resolution ratio (*58*). In this work, the images acquired by using an in vivo fluorescence imaging system and MRI provide important information to demonstrate the active target delivery of dual-responsive neutrobots in mice. The in vivo fluorescence imaging system tracks the dynamic position of neutrobots but cannot recognize a single neutrobot or determine the number of neutrobots in the mice owing to low spatial resolution and tissue-penetrating depth. MRI has a higher tissue-penetrating depth, but its spatiotemporal resolution is still limited. These techniques cannot accomplish the real-time visualization of neutrobot individuals and swarms in vivo with high spatiotemporal resolution nor can they support the future development of neutrobots with self-navigation capacity for practical applications. Therefore, more advanced real-time, multiscale in vivo imaging systems are essential for neutrobot-based robotic systems with self-navigation capacity based on real-time visualization, dynamic path planning, and signal feedback.

The therapeutic effect in the current platform has not reached a substantial advancement over current clinical practice, and thus, future investigations should focus on the systematic majorization of neutrobots-based therapy, including various parameters involving RMF, drug loading, and phagocytosis by NEs. In addition, the emergence and navigation of neutrobot swarms upon exposure to RMF promise direct visualization in vivo owing to the enlarged scale of swarms, which is detectable using current imaging technology. Together, the dual-responsive neutrobots combine the merits of controllable propulsion and swarm intelligence of magnetic swimming microrobots with the chemotaxis and BBB-penetrating capabilities of natural NEs and thus hold considerable promise for active targeted delivery.

MATERIALS AND METHODS

Fabrication of neutrobots and characterization of uptake ratio

Neutrobots were constructed by incubating NEs with EM@nanogels. NEs were incubated with EM@nanogels [EM@nanogels (1 mg ml^{-1}) containing PTX (~57 μg ml^{-1})] in a sterile tube (5×10^5 cells ml^{-1}) at 37°C for 30 min. Neutrobots were obtained after being washed with phosphate-buffered saline twice. The phagocytosis process of NEs was captured using CLSM in a time interval of 15 min. Isothiocyanate isomer I (FITC) was used to label nanogels and EM@nanogels. Flow cytometry was used to study the NEs' cellular uptake of nanogels and EM@nanogels. NEs (5×10^5 cells ml^{-1}) were incubated with nanogels or EM@nanogels (1 mg ml^{-1}) for 30 min at 37°C. After incubation, the excess nanogels or EM@nanogels were removed. The nanogel- or EM@nanogel-loaded NEs were collected and subjected to fluorescence analysis. The resulting fluorescence signal was compared with the original NEs, which served as the control group, and the loading percent of NEs was calculated.

Motion of neutrobots under magnetic field in vitro

The controllable magnetically actuated locomotion of neutrobots was driven by homogeneous RMF generated by a vision-based magnetic navigation system (fig. S8). The system consisted of an optical microscope, a triaxial Helmholtz coil, a National Instruments DAQ (data acquisition) card (NI-PCI-6259) to generate coil-driven inputs of arbitrary waveform signals, and a closed-loop feedback module as a motion planner. The samples containing neutrobots with RPMI 1640 medium (containing 10% FBS) were placed at the center of the triaxial Helmholtz coil and observed under a microscope (Olympus). The motion behavior of neutrobots was recorded using a charge-coupled device (CCD) camera attached on the microscope and analyzed with ImageJ software. The used magnetic field had the intensity of 0 to 18 mT and frequency of 0 to 200 Hz. The input voltages to the Helmholtz coil were 1, 2, and 3 V, corresponding to the intensities of 6, 12, and 18 mT, respectively.

To accomplish the emergence of chain-like neutrobot swarm, the input voltage was manipulated to 3 V, and the frequency was set to 15 Hz. The dynamics of mono-neutrobot, di-neutrobot chain, tri-neutrobot chain, and tetra-neutrobot chain were observed with RMF, and the velocity of neutrobots was calculated by the ImageJ plugin MTrack2. The manipulation of RMF was used to control the motion of neutrobots to the desired trajectory.

Motion of neutrobots against flow under RMF

The microfluidic chip for model blood flow was developed using an intravenous infusion tube and a square quartz tube with an outer width of 1 mm and inner width of 500 μm. The flow channel was fixed in a dish (Cellvis, D35-20-1-N), and the dish was fixed inside the magnetic field coils (fig. S12). The neutrobots and fresh blood were mixed and subsequently introduced into the flow channel. A syringe pump was used to generate flow with controllable flow rate: The volume flow rates of 1.5, 6, and 10.5 μl min^{-1} in the syringe pump resulted in the average flow rates of 100, 400, and 700 μm s^{-1} in the square quartz tube. The motion of neutrobots inside the square quartz tube was observed and recorded using an inverted microscope.

Chemotactic motion

Chemotactic motion of neutrobots was visualized using different channels to create the gradient of chemokine. A PDMS channel with a width of 0.2 mm and length of 5 mm was used for the formation of CG and motion of neutrobots. A cylindrical piece of agarose gel containing 1 μM fMLP was placed at one end of the channel to form a stable gradient of fMLP. Neutrobot motion was recorded with an optical microscope. Ibidi μ-Slide Chemotaxis^{3D} assay was used to investigate the chemotactic motion of neutrobots. Neutrobots were seeded in a channel with collagen I, rat tail. The reservoir at one side of the channel was filled with FBS-free RPMI 1640 medium, and the reservoir at the other side was filled with RPMI 1640 medium containing fMLP (0, 5, 10, 20, 50, and 100 nM). Neutrobots moved within the collagen gel along the CG in the channel. Neutrobot motion was recorded by an optical microscope with CCD, and the trajectories and direction distribution were obtained using the ImageJ plugin Chemotaxis tool. TAD was obtained by analyzing the angle between two neighboring displacements. Motion trajectories of neutrobots were first tracked using an ImageJ plugin, MTrack2, and then a histogram of the turning angle of neutrobots ($n = 600$) during the chemotactic motion was analyzed as the distribution of angle (θ) between $\vec{r}(t + \Delta t)$ and $\vec{r}(t)$, time increment, $\Delta t = 1$ s. Next, the TAD was calculated through fitting with Gaussian distribution. The chemotactic motion profile of NEs was tested and analyzed using the same method as for the neutrobots.

Dual-responsive motion

Rat aorta resected from the thoracic cavity of rats was filled with RPMI 1640 medium containing 10% FBS and placed in a glass slide. A micropipette filled with 1 μM fMLP solution was fixed and used to release fMLP to form a gradient to trigger the chemotaxis of neutrobots. For magnetic propulsion, an RMF with a frequency of 2 Hz was generated before the intravascular injection of neutrobots. Chemotactic motion of neutrobots was then activated by ceasing the magnetic field and adding fMLP. The motion of neutrobots was observed and recorded using a normal optical microscope and analyzed using ImageJ plugin manual tracking and Chemotaxis tool (downloaded from https://ibidi.com/). Movie S10 corresponding with Fig. 6B was processed by "stabilize motion" function of Adobe After Effects to show a clearer view without changing the trajectories of the two neutrobots.

Actively penetrating the model BBB

A Transwell cell culture system (Corning) was used to evaluate the penetration of neutrobots across a model BBB. The model BBB was constructed with bEnd.3 cells using a Transwell cell culture system. Corning Transwell polycarbonate membrane cell culture was placed in a 24-well plate, and a porous membrane was attached at the center of the well plate (photograph in fig. S19 and scheme in fig. S20). The bEnd.3 cells (1×10^5 cells per well) were seeded on the chamber at the top of the Transwell and then cultivated with the medium containing FBS [10% (v/v)] for more than 15 days until a monolayer barrier was formed.

For the control group (NEs or neutrobots), FBS-free RPMI 1640 medium was added to the bottom chamber. The whole system was cultured in 5% CO_2 at 37°C. For the RMF groups (NEs + RMF and neutrobots + RMF), FBS-free RPMI 1640 medium was added to the bottom chamber. The neutrobots were navigated to approach the brain endothelial cell layer upon exposure to RMF with an intensity of 15 mT and frequency of 2 Hz. The whole system was cultured in 5% CO_2 at 37°C in a magnetic field. For the CG groups (NEs + CG and neutrobots + CG), FBS-free RPMI 1640 medium with 10 nM fMLP was added to the bottom chamber to create CG. The Transwell system was cultured in 5% CO_2 at 37°C without magnetic field. For the dual-response (DR) group, the neutrobots were navigated to approach the brain endothelial cell layer upon exposure to RMF with an intensity of 15 mT and frequency of 2 Hz, and FBS-free RPMI 1640 medium with 10 nM fMLP was added to the bottom chamber to create CG. NEs or neutrobots (1×10^6 cells per well) in FBS-free RPMI 1640 medium with the same volume of 100 μl were added to the upper chamber in each group. FBS-free RPMI 1640 medium or FBS-free RPMI 1640 medium with 10 nM fMLP (1 ml) was added to the bottom chamber as the control (neutrobots group and neutrobots + RMF group) or to create CG (neutrobots + CG and neutrobots + DR group). The bottom of the Transwell with different groups was observed and recorded with an optical microscope at 0.5, 1, 2, and 3 hours. At each time, the average number of cells across 10 images was calculated. Then, the number of cells in the bottom chamber was calculated. Each experiment was repeated three times.

CLSM imaging of the dynamic migration process across model BBB

A μ-Slide Membrane ibiPore flow microchannel from Ibidi was applied to establish the BBB model. The bEnd.3 cells (labeled by calcein-AM) were cultivated on the bottom of the chamber, and 10 nM fMLP was added to the bottom of the chamber to create the CG. Neutrobots (1×10^6 cells, labeled by DiI) were subsequently added to the Transwell. The penetration of neutrobots across the model BBB was captured using CLSM (TCS, SP5 II, Leica) in *xyz* mode.

RMF setup for in vivo experiments

The magnetic propulsion of neutrobots in vivo was driven by a home-made giant three-orthogonal Helmholtz coil pair with a navigation system in vitro. The BALB/c nude mice for different treatments were placed into the center of the giant Helmholtz coil. The used intensity was 5 mT, and the rotation frequency was 1 Hz. To carry out magnetic actuation in vivo, the glioma-bearing mice were first anesthetized, and then the neutrobots were injected through the caudal vein. The glioma-bearing mice in the neutrobots + RMF group were placed and fixed into the center of the giant three-orthogonal Helmholtz coil pair and treated with RMF for 1 hour. The dynamics of neutrobots in vivo were imaged using fluorescence imaging and MRI at the interval of magnetic actuation.

SUPPLEMENTARY MATERIALS

robotics.sciencemag.org/cgi/content/full/6/52/eaaz9519/DC1

Methods

Fig. S1. Characterization of Fe_3O_4 NPs.

Fig. S2. TEM image of nanogels.

Fig. S3. Dependence of PTX encapsulated in each milligram nanogels on PTX loading amount.

Fig. S4. CLSM images of EM@nanogels.

Fig. S5. Movement of neutrophils incubated in different suspensions.

Fig. S6. Morphological image of neutrophils.

Fig. S7. CLSM images of neutrophils, neutrobots, neutrophils incubated with nanogels to show cell viability.

Fig. S8. RMF navigation system.

Fig. S9. Velocity of neutrobots (nanogels inside) under RMF with different strength and frequency.

Fig. S10. Motion of neutrobots on the substrate and suspended in liquid under RMF (15 mT, 2 Hz).

Fig. S11. Motion of neutrobots under gradient MF (~800 mT).

Fig. S12. Photograph of the model blood flow system using a fresh blood–filled microfluidic.

Fig. S13. Frequency range of neutrobot swarm formation under RMF (18 mT).

Fig. S14. Simulation of neutrobots' positions in a tetramer swarm in *Y* and *Z* axis change with time.

Fig. S15. Schematic layout of Ibidi μ-Slide Chemotaxis^{3D}.

Fig. S16. Scheme illustration of measurement of TAD.

Fig. S17. Chemotactic motion of neutrophils in CG.

Fig. S18. Velocity of neutrobots on the surface of blood vessel and PDMS substrate under RMF (15 mT, 2 Hz).

Fig. S19. Photograph of actual Transwell setup in 24-well plate.

Fig. S20. Schematic and microscope images of neutrophils and neutrobots going through model BBB.

Fig. S21. CLSM images of EM@nanogel-loaded neutrobots before treated with fMLP or PMA.

Fig. S22. CLSM images show neutrobots deliver EM@nanogels to G422 cells.

Fig. S23. CLSM image of the brain-frozen section of brain harvest from glioma-bearing mouse.

Fig. S24. Helmholtz coil magnetic field device used in animal experiment.

Fig. S25. Targeting ratio of neutrobots to main organs of glioma-bearing mice after different treatment.

Fig. S26. T_2-weighted MRI of blood, neutrobots, and magnetic NPs with different concentration.

Fig. S27. Ultrathin-section TEM images of glioma to show neutrobots inside glioma tissue.

Fig. S28. Statistics of neutrobots in the histosection of glioma.

Fig. S29. Change in the body weight of glioma-bearing mice after different treatment.

Fig. S30. Histological observation of main organs collected from glioma-bearing mice after different treatment.

Movie S1. Schematic illustration for synthesis and dual-responsive active delivery of neutrobots.

Movie S2. Motion of multiple neutrobots moving toward a certain direction under RMF (15 mT, 2 Hz).

Movie S3. Motion of neutrobots on the substrate (blue trajectory) and suspended in liquid (green trajectory) under RMF (15 mT, 2 Hz).

Movie S4. Motion of neutrobots with a wave-like trajectory and star-like trajectory under RMF (15 mT, 2 Hz).

Movie S5. Motion of neutrobots under gradient MF (~800 mT).
Movie S6. Motion of neutrobots against flow under RMF.
Movie S7. Formation of chain from mono-neutrobot to tetra-neutrobots under RMF (18 mT, 15 Hz).
Movie S8. Magnetically powered movement of tetra-neutrobot swarm chain under RMF (18 mT, 15 Hz).
Movie S9. Chemotactic motion of neutrobots along CG.
Movie S10. Dual-responded motion of neutrobots on the blood vessel wall.
Movie S11. Neutrobots moving across the BBB model by chemotactic motion.
Reference (*59*)

REFERENCES AND NOTES

1. J. Li, B. Esteban-Fernández de Ávila, W. Gao, L. Zhang, J. Wang, Micro/nanorobots for biomedicine: Delivery, surgery, sensing, and detoxification. *Sci. Robot.* **2**, eaam6431 (2017).
2. M. Sitti, Miniature soft robots—Road to the clinic. *Nat. Rev. Mater.* **3**, 74–75 (2018).
3. T. E. Mallouk, A. Sen, Powering nanorobots. *Sci. Am.* **300**, 72–77 (2009).
4. J. Wang, W. Gao, Nano/microscale motors: Biomedical opportunities and challenges. *ACS Nano* **6**, 5745–5751 (2012).
5. W. Gao, R. Dong, S. Thamphiwatana, J. Li, W. Gao, L. Zhang, J. Wang, Artificial micromotors in the mouse's stomach: A step toward in vivo use of synthetic motors. *ACS Nano* **9**, 117–123 (2015).
6. G. A. Ozin, I. Manners, S. Fournier-Bidoz, A. Arsenault, Dream nanomachines. *Adv. Mater.* **17**, 3011–3018 (2005).
7. H. Wang, M. Pumera, Fabrication of micro/nanoscale motors. *Chem. Rev.* **115**, 8704–8735 (2015).
8. D. Fan, Z. Yin, R. Cheong, F. Q. Zhu, R. C. Cammarata, C. L. Chien, A. Levchenko, Subcellular-resolution delivery of a cytokine through precisely manipulated nanowires. *Nat. Nanotechnol.* **5**, 545–551 (2010).
9. D. A. Wilson, R. J. M. Nolte, J. C. M. van Hest, Autonomous movement of platinum-loaded stomatocytes. *Nat. Chem.* **4**, 268–274 (2012).
10. B. Esteban-Fernández de Ávila, M. A. Lopez-Ramirez, R. Mundaca-Uribe, X. Wei, D. E. Ramírez-Herrera, E. Karshalev, B. Nguyen, R. H. Fang, L. Zhang, J. Wang, Multicompartment tubular micromotors toward enhanced localized active delivery. *Adv. Mater.* **32**, 2000091 (2020).
11. C. Chen, E. Karshalev, J. Guan, J. Wang, Magnesium-based micromotors: Water-powered propulsion, multifunctionality, and biomedical and environmental applications. *Small* **14**, 1704252 (2018).
12. M. Wan, H. Chen, Q. Wang, Q. Niu, P. Xu, Y. Yu, T. Zhu, C. Mao, J. Shen, Bio-inspired nitric-oxide-driven nanomotor. *Nat. Commun.* **10**, 966 (2019).
13. B. Dai, J. Wang, Z. Xiong, X. Zhan, W. Dai, C.-C. Li, S.-P. Feng, J. Tang, Programmable artificial phototactic microswimmer. *Nat. Nanotechnol.* **11**, 1087–1092 (2016).
14. F. Meng, A. Ortiz-Ambriz, H. Massana-Cid, A. Vilfan, R. Golestanian, P. Tierno, Field synchronized bidirectional current in confined driven colloids. *Phys. Rev. Res.* **2**, 012025 (2020).
15. A. Ghosh, P. Fischer, Controlled propulsion of artificial magnetic nanostructured propellers. *Nano Lett.* **9**, 2243–2245 (2009).
16. J. Cui, T.-Y. Huang, Z. Luo, P. Testa, H. Gu, X.-Z. Chen, B. J. Nelson, L. J. Heyderman, Nanomagnetic encoding of shape-morphing micromachines. *Nature* **575**, 164–168 (2019).
17. W. Wang, S. Li, L. Mair, S. Ahmed, T. J. Huang, T. E. Mallouk, Acoustic propulsion of nanorod motors inside living cells. *Angew. Chem. Int. Ed.* **53**, 3201–3204 (2014).
18. X. Yan, Q. Zhou, M. Vincent, Y. Deng, J. Yu, J. Xu, T. Xu, T. Tang, L. Bian, Y.-X. J. Wang, K. Kostarelos, L. Zhang, Multifunctional biohybrid magnetite microrobots for imaging-guided therapy. *Sci. Robot.* **2**, eaaq1155 (2017).
19. W. Hu, G. Z. Lum, M. Mastrangeli, M. Sitti, Small-scale soft-bodied robot with multimodal locomotion. *Nature* **554**, 81–85 (2018).
20. Y. Alapan, U. Bozuyuk, P. Erkoc, A. C. Karacakol, M. Sitti, Multifunctional surface microrollers for targeted cargo delivery in physiological blood flow. *Sci. Robot.* **5**, eaba5726 (2020).
21. V. M. Kadiri, C. Bussi, A. W. Holle, K. Son, H. Kwon, G. Schütz, M. G. Gutierrez, P. Fischer, Biocompatible magnetic micro- and nanodevices: Fabrication of FePt nano-propellers and cell transfection. *Adv. Mater.* **32**, 2001114 (2020).
22. J. Yu, D. Jin, K.-F. Chan, Q. Wang, K. Yuan, L. Zhang, Active generation and magnetic actuation of microrobotic swarms in bio-fluids. *Nat. Commun.* **10**, 5631 (2019).
23. H. Xie, M. Sun, X. Fan, Z. Lin, W. Chen, L. Wang, L. Dong, Q. He, Reconfigurable magnetic microrobot swarm: Multimode transformation, locomotion, and manipulation. *Sci. Robot.* **4**, eaav8006 (2019).
24. F. Ji, D. Jin, B. Wang, L. Zhang, Light-driven hovering of a magnetic microswarm in fluid. *ACS Nano* **14**, 6990–6998 (2020).
25. S. K. Srivastava, M. Medina-Sánchez, B. Koch, O. G. Schmidt, Medibots: Dual-action biogenic microdaggers for single-cell surgery and drug release. *Adv. Mater.* **28**, 832–837 (2016).
26. A. Servant, F. Qiu, M. Mazza, K. Kostarelos, B. J. Nelson, Controlled in vivo swimming of a swarm of bacteria-like microrobotic flagella. *Adv. Mater.* **27**, 2981–2988 (2015).
27. D. Schamel, A. G. Mark, J. G. Gibbs, C. Miksch, K. I. Morozov, A. M. Leshansky, P. Fischer, Nanopropellers and their actuation in complex viscoelastic media. *ACS Nano* **8**, 8794–8801 (2014).
28. C. K. Schmidt, M. Medina-Sánchez, R. J. Edmondson, O. G. Schmidt, Engineering microrobots for targeted cancer therapies from a medical perspective. *Nat. Commun.* **11**, 5618 (2020).
29. F. Peng, Y. Tu, D. A. Wilson, Micro/nanomotors towards in vivo application: Cell, tissue and biofluid. *Chem. Soc. Rev.* **46**, 5289–5310 (2017).
30. M. Medina-Sánchez, H. Xu, O. G. Schmidt, Micro- and nano-motors: The new generation of drug carriers. *Ther. Deliv.* **9**, 303–316 (2018).
31. M. Hamdi, A. Ferreira, Guidelines for the design of magnetic nanorobots to cross the blood–brain barrier. *IEEE Trans. Robot.* **30**, 81–92 (2014).
32. S. N. Tabatabaei, S. Duchemin, H. Girouard, S. Martel, Towards MR-navigable nanorobotic carriers for drug delivery into the brain, in *2012 IEEE International Conference on Robotics and Automation* (01 May 2012), pp. 727–732.
33. F. Zhang, R. Mundaca-Uribe, H. Gong, B. Esteban-Fernández de Ávila, M. Beltrán-Gastélum, E. Karshalev, A. Nourhani, Y. Tong, B. Nguyen, M. Gallot, Y. Zhang, L. Zhang, J. Wang, A macrophage–magnesium hybrid biomotor: Fabrication and characterization. *Adv. Mater.* **31**, 1901828 (2019).
34. J. Shao, M. Xuan, H. Zhang, X. Lin, Z. Wu, Q. He, Chemotaxis-guided hybrid neutrophil micromotors for targeted drug transport. *Angew. Chem. Int. Ed.* **56**, 12935–12939 (2017).
35. S. Tang, F. Zhang, H. Gong, F. Wei, J. Zhuang, E. Karshalev, B. Esteban-Fernández de Ávila, C. Huang, Z. Zhou, Z. Li, L. Yin, H. Dong, R. H. Fang, X. Zhang, L. Zhang, J. Wang, Enzyme-powered Janus platelet cell robots for active and targeted drug delivery. *Sci. Robot.* **5**, eaba6137 (2020).
36. Z. Wu, T. Li, J. Li, W. Gao, T. Xu, C. Christianson, W. Gao, M. Galarnyk, Q. He, L. Zhang, J. Wang, Turning erythrocytes into functional micromotors. *ACS Nano* **8**, 12041–12048 (2014).
37. V. Papayannopoulos, Neutrophil extracellular traps in immunity and disease. *Nat. Rev. Immunol.* **18**, 134–147 (2018).
38. S. K. Jorch, P. Kubes, An emerging role for neutrophil extracellular traps in noninfectious disease. *Nat. Med.* **23**, 279–287 (2017).
39. S. de Oliveira, E. E. Rosowski, A. Huttenlocher, Neutrophil migration in infection and wound repair: Going forward in reverse. *Nat. Rev. Immunol.* **16**, 378–391 (2016).
40. T. H. C. de Oliveira, P. E. Marques, P. Proost, M. M. M. Teixeira, Neutrophils: A cornerstone of liver ischemia and reperfusion injury. *Lab. Invest.* **98**, 51–62 (2018).
41. J. Xue, Z. Zhao, L. Zhang, L. Xue, S. Shen, Y. Wen, Z. Wei, L. Wang, L. Kong, H. Sun, Q. Ping, R. Mo, C. Zhang, Neutrophil-mediated anticancer drug delivery for suppression of postoperative malignant glioma recurrence. *Nat. Nanotechnol.* **12**, 692–700 (2017).
42. D. Chu, X. Dong, X. Shi, C. Zhang, Z. Wang, Neutrophil-based drug delivery systems. *Adv. Mater.* **30**, e1706245 (2018).
43. C. Tang, C. Wang, Y. Zhang, L. Xue, Y. Li, C. Ju, C. Zhang, Recognition, intervention, and monitoring of neutrophils in acute ischemic stroke. *Nano Lett.* **19**, 4470–4477 (2019).
44. W. M. Li, S. Y. Chen, D. M. Liu, In situ doxorubicin–CaP shell formation on amphiphilic gelatin–iron oxide core as a multifunctional drug delivery system with improved cytocompatibility, pH-responsive drug release and MR imaging. *Acta Biomater.* **9**, 5360–5368 (2013).
45. W. Gao, R. H. Fang, S. Thamphiwatana, B. T. Luk, J. Li, P. Angsantikul, Q. Zhang, C.-M. J. Hu, L. Zhang, Modulating antibacterial immunity via bacterial membrane-coated nanoparticles. *Nano Lett.* **15**, 1403–1409 (2015).
46. H. A. Faruque, E.-S. Choi, J.-H. Kim, S. Kim, E. Kim, In vivo removal of radioactive cesium compound using Prussian blue-deposited iron oxide nanoparticles. *Nanomedicine* **14**, 3143–3158 (2019).
47. K. I. Morozov, A. M. Leshansky, The chiral magnetic nanomotors. *Nanoscale* **6**, 1580–1588 (2014).
48. J. J. Abbott, K. E. Peyer, M. C. Lagomarsino, L. Zhang, L. Dong, I. K. Kaliakatsos, B. J. Nelson, How should microrobots swim? *Int. J. Robot. Res.* **28**, 1434–1447 (2009).
49. K. E. Peyer, L. Zhang, B. J. Nelson, Bio-inspired magnetic swimming microrobots for biomedical applications. *Nanoscale* **5**, 1259–1272 (2013).
50. Z. Lin, X. Fan, M. Sun, C. Gao, Q. He, H. Xie, Magnetically actuated peanut colloid motors for cell manipulation and patterning. *ACS Nano* **12**, 2539–2545 (2018).
51. H. Xu, M. Medina-Sánchez, M. F. Maitz, C. Werner, O. G. Schmidt, Sperm micromotors for cargo delivery through flowing blood. *ACS Nano* **14**, 2982–2993 (2020).
52. K. P. Ivanov, M. K. Kalinina, Y. I. Levkovich, Blood flow velocity in capillaries of brain and muscles and its physiological significance. *Microvasc. Res.* **22**, 143–155 (1981).
53. X. M. O'Brien, A. J. Loosley, K. E. Oakley, J. X. Tang, J. S. Reichner, Technical Advance: Introducing a novel metric, directionality time, to quantify human neutrophil chemotaxis as a function of matrix composition and stiffness. *J. Leukoc. Biol.* **95**, 993–1004 (2014).
54. Y. Omidi, L. Campbell, J. Barar, D. Connell, S. Akhtar, M. Gumbleton, Evaluation of the immortalised mouse brain capillary endothelial cell line, b.End3, as an in vitro

blood–brain barrier model for drug uptake and transport studies. *Brain Res.* **990**, 95–112 (2003).
55. T. M. Keenan, A. Folch, Biomolecular gradients in cell culture systems. *Lab Chip* **8**, 34–57 (2008).
56. D. L. Bratton, P. M. Henson, Neutrophil clearance: When the party is over, clean-up begins. *Trends Immunol.* **32**, 350–357 (2011).
57. A. Mantovani, P. Allavena, A. Sica, F. Balkwill, Cancer-related inflammation. *Nature* **454**, 436–444 (2008).
58. S. Pané, J. Puigmartí-Luis, C. Bergeles, X.-Z. Chen, E. Pellicer, J. Sort, V. Počepcová, A. Ferreira, B. J. Nelson, Imaging technologies for biomedical micro- and nanoswimmers. *Adv. Mater. Technol.* **4**, 1800575 (2019).
59. S. Sun, H. Zeng, D. B. Robinson, S. Raoux, P. M. Rice, S. X. Wang, G. Li, Monodisperse MFe_2O_4 (M = Fe, Co, Mn) nanoparticles. *J. Am. Chem. Soc.* **126**, 273–279 (2004).

Funding: This work was financially supported by the National Nature Science Foundation of China (grant no. 21972035) and Heilongjiang Providence Nature Science Foundation of China (grant no. YQ2019E018). **Author contributions:** Q.H. and Z.W. conceived the project. Q.H., Z.W., and C.G. supervised the studies. H.Z., Z.L., and C.G. prepared and characterized the neutrobots. T.L. constructed the Helmholtz coil device. H.Z., T.L., X.F., and H.X. performed magnetic movement experiments. H.Z. drew the schematic illustrations. H.Z., Z.L., and Y.P. conducted in vivo experiments. H.Z., Z.W., and Q.H. interpreted data and wrote the manuscript. All authors reviewed the manuscript. **Competing interests:** The authors declare that they have no competing financial interests. **Data and materials availability:** All data needed to evaluate the conclusions in the paper are present in the paper or the Supplementary Materials.

Submitted 12 September 2020
Accepted 26 February 2021
Published 24 March 2021
10.1126/scirobotics.aaz9519

Citation: H. Zhang, Z. Li, C. Gao, X. Fan, Y. Pang, T. Li, Z. Wu, H. Xie, Q. He, Dual-responsive biohybrid neutrobots for active target delivery. *Sci Robot.* **6**, eaaz9519 (2021).

Science Robotics

Dual-responsive biohybrid neutrobots for active target delivery

Hongyue Zhang, Zesheng Li, Changyong Gao, Xinjian Fan, Yuxin Pang, Tianlong Li, Zhiguang Wu, Hui Xie, and Qiang He

Sci. Robot. **6** (52), eaaz9519. DOI: 10.1126/scirobotics.aaz9519

Science Robotics (ISSN 2470-9476) is published by the American Association for the Advancement of Science. 1200 New York Avenue NW, Washington, DC 20005. The title *Science Robotics* is a registered trademark of AAAS.